

Benchmarking Framework for SAR Despeckling

Gerardo Di Martino, *Member, IEEE*, Mariana Poderico, Giovanni Poggi,
Daniele Riccio, *Senior Member, IEEE*, and Luisa Verdoliva

Abstract—Objective performance assessment is a key enabling factor for the development of better and better image processing algorithms. In synthetic aperture radar (SAR) despeckling, however, the lack of speckle-free images precludes the use of reliable full-reference measures, leaving the comparison among competing techniques on shaky bases. In this paper, we propose a new framework for the objective (quantitative) assessment of SAR despeckling techniques, based on simulation of SAR images relevant to canonical scenes. Each image is generated using a complete SAR simulator that includes proper physical models for the sensed surface, the scattering, and the radar operational mode. Therefore, in the limits of the simulation models, the employed simulation procedure generates reliable and meaningful SAR images with controllable parameters. Through simulating multiple SAR images as different instances relevant to the same scene we can therefore obtain, a true multilook full-resolution SAR image, with an arbitrary number of looks, thus generating (by definition) the closest object to a clean reference image. Based on this concept, we build a full performance assessment framework by choosing a suitable set of canonical scenes and corresponding objective measures on the SAR images that consider speckle suppression and feature preservation. We test our framework by studying the performance of a representative set of actual despeckling algorithms; we verify that the quantitative indications given by numerical measures are always fully consistent with the rationale specific of each despeckling technique, strongly agrees with qualitative (expert) visual inspections, and provide insight into SAR despeckling approaches.

Index Terms—Quality assessment, SAR simulation, speckle reduction, synthetic aperture radar (SAR).

I. INTRODUCTION

WITH the increasing diffusion of remote-sensing products, with fleets of satellites delivering a huge number of images of the Earth's surface each day, the use of automatic analysis tools is ever more widespread. Homeland security, environmental protection, land resource management, to cite just some of the major applications, require the analysis of a very large number of images, far exceeding the capacity of trained human personnel. The performances of many image processing tasks, such as image segmentation, or target detection and classification, heavily depend on the quality of the source images, which should provide reliable and easy to extract information. However, this is not the case of (single-

look) synthetic aperture radar (SAR) images, given the inherent presence of speckle that can easily disguise small targets and hamper, in general, the detection of relevant features. On the other hand, SAR is such an important source of information, providing high-resolution images with all weather and illumination conditions, and complementing the set of features sensed by optical instruments, that renouncing it is simply unthinkable. These considerations motivate the increasingly intense quest for reliable despeckling techniques, which succeed in removing most of the speckle without impairing potentially valuable image data. Indeed, image despeckling has been an active field of research for almost 30 years, and many new algorithms are proposed each year that appear to provide better and better performance. The assessment of performance, however, is by itself a very relevant and still open problem in SAR despeckling. No agreed upon protocol exists, to these authors' knowledge, to measure performance, nor there is a publicly available set of benchmark images that allows for an objective comparison of algorithms through simple and replicable experiments. These considerations motivate this paper,¹ aimed at proposing a new approach to performance assessment of despeckling techniques and providing a practical tool for the interested community.

Before going into any technical detail, the very same meaning of performance, in this context, must be better clarified. SAR images are analyzed by human experts or by automatic programs to extract some information of interest for the final application. To this end, complex tasks are performed on the image, such as segmentation, detection, classification, parameter estimation, and compression. Therefore, the effectiveness of a given despeckling algorithm should be measured *a posteriori*, by evaluating the success of the subsequent processing tasks [2]–[5]. Therefore, for example, an algorithm could be credited to perform a good image despeckling if the processed images allow for an easier detection of targets, or a more efficient transmission on a narrowband channel, and so on. Although this end-to-end approach is probably correct, it is also obviously impractical, except for some niche applications, as results depend strongly on the implementation of subsequent tasks (detection, classification, and so on) and on the experimental conditions (sensor parameters, observed scene, and so on). At the other end of the spectrum, there is the totally subjective approach to image quality assessment, relying on a panel of experts working in controlled experimental conditions that evaluate or rank filtered images based on their field experience [6], [7]. This kind of assessment would be really precious, given the ability of trained human personnel to consider features that easily elude automatic measurements, and indeed there is a regrettable shortage of this

Manuscript received May 24, 2012; revised January 17, 2013; accepted March 4, 2013. Date of publication May 13, 2013; date of current version December 17, 2013. This work was supported in part by the Science and Technology Pole, University of Naples Federico II, in the framework of the F.A.R.O. Program - IV Session 2012.

The authors are with the Dipartimento di Ingegneria Elettrica e delle Tecnologie dell'Informazione, Università di Napoli Federico II, Napoli 80125, Italy (e-mail: gerardo.dimartino@unina.it; mariana.poderico@unina.it; poggi@unina.it; daniele.riccio@unina.it; verdoliva@unina.it).

Color versions of one or more of the figures in this paper are available online at <http://ieeexplore.ieee.org>.

Digital Object Identifier 10.1109/TGRS.2013.2252907

¹Preliminary results of this research are presented in [1].

kind of researches. However, it would also be very expensive, requiring the prolonged help of several expert interpreters under controlled conditions, and nonreplicable, because of its inherently subjective nature.

Once barred the above approaches, both related, directly or indirectly, to the usefulness of images for the final applications, one is left with the (seemingly) less ambitious, but still valuable, and conceptually sound, goal of objectively measuring the fidelity of the despeckled image with respect to a reference speckle-free image. The problem, of course, is that no such thing as a speckle-free version of a given real-world SAR image exists, barring the use of true full-reference measures. In some very simple cases, one can guess the clean image by visual inspection, and then compute some meaningful measures of performance, like the equivalent number of looks (ENL) in the presence of a flat homogeneous region, or some edge-preservation measures [8]–[10] when a straight border between homogeneous regions exists. However, this method cannot work in regions that exhibit texture, or multiple and variously oriented edges, or man-made structures. The approach commonly used in the literature to cope with this problem is to start from a virtually noiseless image (typically a natural optical image), which takes the role of the clean reference, and superimpose a speckle field with proper statistics to it. Leaving aside, for the moment, the problem of correctly modeling the speckle, the major weak point of this approach lies in the fact that these images are erroneous substitutes for the desired clean reference. Under a physical viewpoint there is no doubt about it, as even optical remote-sensing images differ from SAR images for sensed quantity, operational wavelengths, resolution, imaging modalities, and so on. Even neglecting all this, and focusing only on the final products, seen as mere arrays of numbers, the statistics of a SAR image are obviously very different from those of other types of images, for dynamics, gray-level distribution, spatial correlation, power spectral density, and so on.

Despite all these drawbacks, the simulative approach has some strong positive sides, first of all the full reproducibility of experiments and the ability to provide an objective assessment of performance. One only needs to define in a meaningful way a clean SAR image, and find a way to generate it. Stated on physical bases, a speckle-free SAR image sounds like an oxymoron. For natural areas, speckle is the SAR image (coherent) contribution because of subresolution surface roughness; however, a significant radar return is acquired only if the surface is rough at electromagnetic wavelength scales. Accordingly, a speckle-free image could be obtained only if the SAR image could not! A different perspective is then required; a valuable hint to define speckle-free images comes from the despeckling literature itself, where the more common performance measure, the ENL, suggests that the goal of any despeckling technique is to obtain the infinite-look version of the image under analysis. Ideally, if we are able to collect an arbitrarily large number of independent SAR images of the same scene, taken with exactly the same system parameters and in the same conditions, we could carry out a true multilook (i.e., without resorting to spatial averages) with an arbitrarily large number of looks L . We can therefore think of the clean

reference as the limit of this image as L grows toward infinity. Of course, such an image cannot be produced by a real-SAR system, because of the prohibitive challenge posed by the invariance hypotheses. However, we can follow this line of thinking, and obtain some valuable results, in a simulative context, but of physical nature now, rather than statistical.

Indeed, if we were able to describe in detail the imaged region on the ground, including its 3-D geometry at all scales of interest (the minimum spatial scale being of the order of the electromagnetic wavelength), and its local electromagnetic properties, and also to replicate with reasonable accuracy the imaging process of a SAR system, we could obtain a SAR image with the same information content and characteristics of the image provided by a real system. Of course, this process could be repeated at will, producing an arbitrary number of looks of the same scene, differing only in the speckle component originated by very small scale details that can be described only in terms of random processes. Therefore, this physical simulation would solve the problem of the clean infinite-look reference image at its root.

It goes by itself that this approach, as it is described, calls for technological and scientific tools that are well beyond the current state-of-the-art. Both the faithful simulation of a SAR imaging system and a thorough description of a real-ground scene are tasks of prohibitive complexity. However, if we scale back the goal to that of simulating a certain number of basic canonical scenes, which can provide reliable indications of the actual performance in more complex scenarios, the problem becomes manageable with well-established tools. These topics are the object of intense research and rapid advances recently, and researchers of this group developed both accurate models of natural and man-made surfaces, and a complete SAR system simulator that has proven reliable in many practical tests. We are therefore in the position to propose and actually implement a new tool for the assessment of despeckling techniques via physical simulation, based on a set of canonical scenes and of related objective performance measures. Such measures, however, while representing a valuable help for the end user, are not substitute for visual inspection by an expert interpreter, and replacing human experts is declaredly beyond the scope of this paper.

In the following sections, we analyze in some depth the various elements that are relevant for the proposed tool. In Section II, we describe the SAR simulator used in the experiments, pointing out its potential and inherent limitations. In Section III, we review the major ideas and approaches in despeckling, as well as the most common performance measures used in the field. Section IV deals with the set of canonical scenes and the associated distortion measures, selected to test specific strengths and weaknesses of the tested techniques. In Section V, we briefly describe the selected techniques and comment experimental results. Finally, Section VI summarizes conclusions and outlines future research.

II. SAR IMAGE SIMULATION

The simulation framework introduced in this section allows us generating a wide set of canonical SAR images, which can be used as a meaningful test-bed to define objective quality

measures and assess the performances of the despeckling techniques.

A. Motivations

To provide a test-bed for the objective performance assessment of despeckling techniques, we propose to generate SAR images relevant to canonical scenes by means of simulation. From the viewpoint of speckle filtering, SAR signal simulation provides some major advantages. First of all, it represents the best way to obtain a wide set of canonical samples of actual SAR data. In addition, it provides a reliable and effective method to obtain speckle-free images, necessary for the full-reference measurement of filters' performance. At least in principle, the filter should remove as much speckle as possible from the data and, therefore, to assess its effectiveness one needs to compute some measures of the distance between the output image and the ideal speckle-free reference.

However, even the definition of a SAR image without speckle is a nontrivial issue. Although in classical signal theory the noise is described as a disturbing signal distorting the original noise-free one, in the SAR case, the speckle is an intrinsic characteristic of the original signal, thus implying that the speckle-free image is a distorted version of the original one. The presence of speckle is due to the microscopic characteristics of the observed surface, i.e., to its details at spatial scales lower than the resolution one [11], [12]. Anyway, often the postprocessing (e.g., segmentation, classification, and target detection) performed on SAR data pertains only to the macroscopic features, i.e., to spatial scales greater than the resolution one. Hence, for postprocessing purposes, we can define a clean image as an image whose macroscopic features are not affected by the presence of speckle, i.e., an infinite-resolution version of the image under analysis.

Through the SAR raw signal simulator (SARAS) [13] described in the following, we are able to obtain a SAR image presenting a finite but very large number of looks, thus approximating with arbitrary precision the above defined clean image. In particular, we generate reference images by averaging 512-independent intensity SAR images, which guarantees a much stronger reduction of speckle than that provided by the best techniques known in the literature. It is worth underlining that such a goal cannot be reasonably met with real-SAR images, because of technical hurdles, and that the final simulated image is not affected by any loss in spatial resolution, unlike with other procedures, also referred to as multilooking, but based on spatial averages.

The proposed simulator is based on sound geometrical and electromagnetic models for the evaluation of the reflectivity function of the scene and on a model for the transfer function of the system, which are used for the evaluation of the raw signal. These models are not dependent on the used despeckling technique, thus allowing an objective comparison of the selected filtering techniques. The models used for simulation are briefly outlined in the following, paying particular attention to geometric, electromagnetic, and radar parameters of interest.

B. Simulation Procedure

Let x and r be the independent space variables, standing, respectively, for azimuth and range. Through using primed coordinates for the independent variables of the SARAS, $s(x', r')$, this can be expressed as follows [13]:

$$s(x', r') = \iint \gamma(x, r) g(x' - x, r' - r; r) dx dr \quad (1)$$

where $\gamma(x, r)$ is the reflectivity pattern of the scene, and $g(x' - x, r' - r; r)$ is the unit impulse response of the SAR system [13]. For the evaluation of the reflectivity function, electromagnetic scattering models, providing a solution that is function of the considered sensor and surface parameters, are used. First of all, the description of the macroscopic aspects of the surface at the scale of the sensor resolution is required: this is accomplished by providing as input to the simulator a digital elevation model (DEM). The behavior of the DEM is then approximated using a two-scale model [13], i.e., using plane facets, over which a microscopic random roughness is superimposed. Hence, the mean square value of the backscattered field can be evaluated providing an adequate stochastic description of the microscopic roughness. This random roughness can be described by using different parameters resulting from the introduction of different models for the geometry of the surface [14]: in this paper, when a natural terrain is considered, the roughness is supposed to be effectively described through a fractal fractional Brownian motion (fBm) process [14], i.e., using only two independent parameters, the Hurst coefficient H and the topography T [m]. Conversely, when the simulation of buildings is in order, the surface surrounding the building is assumed to be man-made (e.g., asphalt) and the roughness is described through classical geostatistical parameters, the height standard deviation, σ_h [m], and the correlation length, l_h [m]: the use of this model allows us evaluating in closed form the multiple reflection contributions, which are typical of urban areas [15]. Finally, to complete the description of the surface also the relative dielectric constant ϵ and the conductivity σ [S/m] of the observed surfaces must be provided as input to the simulator.

Whenever a natural terrain is considered, the small perturbation model, with the appropriate power law spectrum, is used for the evaluation of the reflectivity function of the surface [14]. Conversely, for the evaluation of the reflectivity relevant to an isolated building, to compute in closed form the multiple reflection contributions, geometrical optics or physical optics solutions are required [15]. The reflectivity function is evaluated in a ground range—azimuth reference system and is necessary to project it in the sensor-centered slant range—azimuth reference system. Once this transformation is performed, the obtained reflectivity function can be filtered according to the impulse response of the SAR system, providing as output the raw signal, as shown in (1). To compute the impulse response, the radar and orbital parameters are needed: pulse repetition frequency, chirp duration and bandwidth, satellite height and velocity, and so on. After focusing, the obtained raw signal provides the final simulated SAR image.

With regard to the speckle phenomenon, its presence is considered in the simulator through the above-introduced

two-scale model for the imaged surface. In this approach the spatial scales smaller and larger than the resolution are differently treated: in particular, the signal macroscopic behavior is considered through the computation of the scattering from plane facets locally approximating the considered surface; electromagnetic roughness parameters of each facet are assumed known; the mean square value of the signal, and hence the normalized radar cross section [13], is evaluated through electromagnetic models adequate for the computation of the scattering from rough surfaces, as described above. The microscopic behavior, which determines the presence of speckle, is considered through a statistical model: in particular, assuming the speckle can be considered as fully developed [11], [12], the amplitude value obtained for each facet is multiplied by one realization of a Rayleigh random variable. Considering the speckle contribution at this early point of simulation guarantees that speckle is filtered by the SAR system impulse response just like the signal is. Therefore, the simulated image exhibits the expected spatial properties of a real-world SAR image, which is not the case when the speckle is superimposed on a pixel basis over the final simulated image [16].

Through the above-described framework we are able to provide a wide set of simulation products, spanning from the reflectivity function to the single-look complex (SLC) image. In this paper, we are interested in intensity images, i.e., the square modulus of the SLC image, which is usually simply referred to as SAR image. Analyzing this product, significant features of the observed scene can be visually inspected and effectively processed to retrieve relevant information.

III. OVERVIEW ON SAR DESPECKLING

Here, we try to provide an overview of the major ideas relevant to SAR despeckling and to the assessment of filtered-image quality. Techniques applicable to a single one-look (i.e., full-resolution) SAR image are considered. The analysis of the filtering methods will allow us to concisely describe the few techniques selected in the experimental part as a representative set of the available ones, and position them in the literature, while the study of the quality assessment will help us to define the proposed performance measures on simulated SAR images.

A. Despeckling Techniques

Major trends in SAR despeckling closely follow the developments in additive white Gaussian noise (AWGN) denoising, with most ideas drawn from the more mature AWGN field and adapted to the challenging special case of speckle noise. Indeed, despeckling techniques typically convert the multiplicative noise problem to an additive one, by resorting to a log-transformation or by rewriting the observable as the sum of the information signal plus signal-dependent noise. The first solution, known as the homomorphic approach, allows one to apply with minor modifications all AWGN techniques, although the results are affected by the distortion of the image dynamics and the non-Gaussian nature of the noise. The second approach is more promising, in theory, but also more complex to deal with, and results do not always live

up to the expectations. We will not discuss further the relative advantages of these two models, focusing instead on the major algorithmic approaches and grouping (loosely) the techniques in three broad categories: 1) spatial; 2) wavelet-based; and 3) nonlocal filtering. In addition, we will not analyze in depth any technique, because in this context, we are only interested in the rationale of each approach and its typical pros and cons.

Despeckling techniques working in the spatial-domain estimate the signal by means of a weighted average of samples in a small window centered on the target pixel. Spatial multilook, still much used by practitioners for both despeckling and pixel-size equalization, can be regarded as a very primitive form of spatial-domain filtering, with equal weights in the window. It is therefore a low-pass filter, which cuts medium-to-high frequencies, thus reducing noise but also all high-frequency signal components associated with edges, man-made structures, natural textures. Multilook epitomizes therefore the typical problem of spatial-domain filters, that is, the loss of resolution in the despeckled signal corresponding to the suppression of high-frequency signal components. The resulting artifacts can be spotted easily by computing the image of ratio between original and speckled images, as signal-related structures superimposed to the uncorrelated speckle. Needless to say, filters proposed in the scientific literature, e.g. [17]–[19], are much more sophisticated than spatial multilook. Weights are computed based on accurate statistical models of signal and noise and, especially important, are modified adaptively to consider the local statistics of the image. Therefore, intense smoothing is carried out only in homogeneous regions, while detail-rich areas, likely associated with valuable signal components, undergo a lighter treatment. Indeed, the segmentation of the image, either implicit or explicit, in homogeneous, heterogeneous, and strongly heterogeneous (man-made) regions, is one of the main tools that help reducing filtering artifacts. Several efforts are done to improve the adaptive local filtering, as the techniques proposed in [20], where the local coefficient of variation is used to tell apart regions with different level of homogeneity, or in [21], which not only inhibits smoothing near edges but tries also to enhance them. Although enhanced filters have the potential to better preserve texture and edges, distinguishing homogeneous regions from texture or edges is a difficult task, and recently, research is focusing on this topic [22], [23].

Following the advent of wavelet transform, with all its variants and further developments, there was a significant leap forward in AWGN denoising initially, and then SAR despeckling. Wavelets are very well-suited to represent images efficiently as most of the information content is captured by a relatively small number of coefficients, typically the baseband, and some detail coefficients related to sharp transitions in the image. On the contrary, assuming orthogonal transforms, white noise keeps being white and evenly distributed on all coefficients. Therefore, it is relatively easy to tell apart coefficients carrying information about the signal from those, generally smaller, which contain only noise. Plain scalar thresholding of wavelet coefficients already provides a surprisingly good performance [24], [25], especially if a shift-invariant undecimated wavelet is used. Encouraged by such good

results, several researchers proposed improved wavelet-domain techniques, using more sophisticated transforms, considering interband coefficient dependencies, and replacing deterministic thresholding with statistical shrinkage. Indeed, most of the techniques proposed in the last few years for SAR despeckling resort to statistical wavelet shrinkage with a maximum *a posteriori* (MAP) Bayesian approach, and focus on the selection of the most suitable prior for the signal coefficients [26]–[30]. In general, it seems safe to say that wavelet-based algorithms guarantee a better overall performance than spatial-domain techniques, and a superior ability to preserve signal resolution. Nonetheless, they present their peculiar kind of artifacts, in the form of ringing near the edges, or isolated patterns in flat areas of the image, which can result visually annoying.

Recently, nonlocal filtering is drawing a great deal of attention. It is a new way to carry out spatial-domain denoising. The main idea is to estimate the target pixel based on a carefully selected set of pixels: not just those closest to the target but those more likely to have the same underlying signal. The idea is not so new, dating back to the 1980s with the neighborhood filter, and later the bilateral filter, but only very recently, with the nonlocal means (NLM) algorithm [31] it proved its effectiveness and spawned intense research. In NLM, the target pixel is estimated as a weighted sum of all neighboring pixels, with weights that depend on the expected similarity between the target and the predictors. Such a similarity is measured, in turn, based on the patches surrounding each pixel. This idea is further developed in block-matching 3-D (BM3D) [32] where only a few pixels with the most similar context are used for the estimation. In addition, BM3D resorts to wavelet-based thresholding, using the best tools from both approaches and providing the best performance to date. It is instructive to think of NLM and BM3D as clever attempts to mimic a true statistic average. Through selecting as predictor those pixels that have the same context as the target, they sort of draw independent samples from the same abstract random process and average them. Both NLM and BM3D are extended to the SAR case [33]–[37]; in particular, in [33] and [36], a suitable similarity measure, related to the speckle statistics, is used in place of the original Euclidean distance valid for AWGN, and other processing steps are modified to consider the specificity of the new domain. Obviously, the predictor selection is influenced by noise itself, especially in flat areas of the image, which can be dangerously self-referential. As a matter of fact, the typical artifacts encountered with this kind of algorithms are the so-called ghosts, structured signal-like patches that appear in flat areas, originated by random noise and reinforced through the patch selection process.

B. Quality Assessment

In general, a good SAR despeckling technique should have the following characteristics [38]:

- 1) speckle reduction in homogeneous areas;
- 2) scene feature preservation (such as texture, edges, point target, and urban areas);
- 3) radiometric preservation;
- 4) absence of artifacts.

To assess the capacity of a filter to achieve such results, a set of suitable measures are used in the literature, which can be classified as no-reference measures (applied on real-world SAR images) and full-reference measures (when a reference SAR image is generated by simulation).

1) *No-Reference Measures*: Lacking a reference, such measures make sense only if referred to areas of the SAR image that can be clearly characterized in terms of their signal content as homogeneous, heterogeneous, or extremely heterogeneous regions.

Homogeneous regions (constant and weakly textured areas) are the most simple to analyze as in these areas the randomness of the observed signal is only caused by speckle, which is fully developed, and for each pixel the multiplicative noise model is valid

$$z = x \cdot u \quad (2)$$

where z is the detected intensity, x is the speckle-free reflectance, and u considers the speckle that can be modeled as Gamma distributed with unit mean and variance $= 1/L$, where L is the number of looks. A very common tool used in the literature to measure speckle suppression is the ENL [38]

$$\text{ENL} = \frac{\mu_z^2}{\sigma_z^2} \quad (3)$$

with μ_z and σ_z the estimated mean and standard deviation of the signal, which is the number of single-look images that should be incoherently averaged to obtain equivalent despeckling in perfectly uniform regions. The larger the ENL the better the speckle suppression, with infinity corresponding to ideal filtering. In a homogeneous region, one can also evaluate the radiometric preservation by comparing the value of the local mean backscattering reflectivity in the original and filtered images. A successful speckle reducing filter should not significantly alter the mean intensity within a homogeneous region [20]. Another method of investigating the despeckling performance is to check the ratio between the noisy and the filtered images. For ideal filtering, the ratio image should be pure speckle. Thus, its mean should equal one, and its variance should be the inverse of the number of looks [39]. In addition, this comparison provides information regarding a possible bias and whether the speckle is insufficiently filtered (the variance is lower than the theoretical value) or the scene texture is smoothed (the variance becomes larger than the theoretical value) [6].

When dealing with heterogeneous regions (textured areas, edges) the analysis becomes more complex. Texture, which represents the intrinsic spatial variability of a natural scene, is a precious feature to discriminate among different land-use types. Measuring its preservation, however, is not an easy task, and one must settle for the less ambitious goal of studying some synthetic indicators, like the coefficient of variation, $C_x = \sigma_x / \mu_x$, which considers the region heterogeneity. Good texture preservation can be obtained only if the coefficient of variation $C_{\hat{x}}$ estimated for the filtered image by means of spatial averages is close to the value expected for the original image [40]. If signal and speckle are independent, and the latter has unit mean, the expected value of C_x can be computed

as follows:

$$C_x = \sqrt{\frac{C_z^2 - C_u^2}{1 + C_u^2}} \quad (4)$$

where C_z is estimated on the observed image z , and C_u equals the standard deviation of the speckle. A critical point of this measure is the selection of an area of constant statistical behavior, so as to actually measure only intratexture and not also intertexture variability [41]. For what concerns edges, one can apply an edge detector on the filtered images and observe the resulting edge map. In addition, the visual inspection of the ratio image can provide information on the degree of edge-preservation in a region, as the presence of structures in it indicates that they are filtered out from the original data. The ratio image can also give important indications on filtering artifacts [38], often not so visible in the filtered image. In other approaches, despeckling quality is judged based on the results of subsequent tasks, such as classification or segmentation, but these are obviously application-dependent and hence not very general.

Finally, extremely heterogeneous areas, such as point targets, strong edges, or buildings, where the speckle does not obey to a fully developed model, should not be filtered at all, and their original value should be preserved. The research on this kind of regions concentrated mostly on determining experimentally the target response by the analysis of real-world SAR images containing one or more corner reflectors [18], [20].

2) *Full-Reference Measures*: The performance assessment becomes much simpler when a clean reference x is available. In the literature, both natural optical images and synthetic images with simple features such as uniform regions, textures, edges or strong scatterers [42] are used as references. Synthetic SAR images are then generated by applying a fully developed speckle field. In this case, one can easily compute all sorts of full-reference global distortion measures on the filtered image \hat{x} , from the traditional mean-square error (MSE)

$$\text{MSE}(x, \hat{x}) = \text{E}[(x - \hat{x})^2] \quad (5)$$

with $\text{E}[\cdot]$ denoting statistical mean, and related quantities like the signal-to-noise ratio (SNR)

$$\text{SNR}(x, \hat{x}) = 10 \log_{10} \frac{\text{Var}(x)}{\text{MSE}(x, \hat{x})} \quad (6)$$

or the peak SNR, up to most recent measures, like the structural similarity index [43], which try to provide more meaningful information about the closeness of two images. The proposed measures can be calculated globally or locally, if one is interested on the performance on specified areas. Through the clean reference, several objective measures are proposed to assess the edge-preservation capacity of the filters. In particular, one can generate synthetic images with edges of different slope, orientation and thickness and define indexes on a certain region of interest. This is the case of edge-preservation index (EPI) [44], defined as follows:

$$\text{EPI} = \frac{\sum_{i=1}^n |\hat{x}_{i,1} - \hat{x}_{i,2}|}{\sum_{i=1}^n |x_{i,1} - x_{i,2}|} \quad (7)$$

where $x_{i,1}$, $x_{i,2}$, $\hat{x}_{i,1}$, and $\hat{x}_{i,2}$ are the values of the reference and filtered images, respectively, observed on the one-pixel wide lines on both sides of the edge. Larger values correspond to a better edge retaining ability of the filter. Recently, a modified version was proposed in [23] called edge-preservation degree based on ratios rather than differences. Alternatively, one can evaluate the correlation index [45], called β -index or edge-correlation factor, between the high-pass versions of the original and filtered images. All these indexes, although quite empirical, provide some indications on the edge-preservation ability of the filter. A deeper analysis can be conducted by examining the gray-level histograms for synthetic images with a single edge [46], observing the edge profile [47], [48] or the second-order correlation contours (SOGLC matrix) [46]. An approach closer to the applications for measuring edge-preservation ability involves the analysis of the edge map obtained with a specific edge detector [18]. The edge map, is an intermediate product in many image segmentation and classification algorithms. To this end, one can resort to the figure of merit (FOM), introduced by Pratt [49], which measures the distance of a given edge map from the reference edge map, penalizing both the suppression of true edges and the detection of false ones.

IV. PROPOSED FRAMEWORK

Almost all the measures outlined in previous section make sense when referred to specified areas of the image. Indeed, when they are used for actual SAR images, it is necessary to identify the regions of interest based on indicators like the coefficient of variation [6]. Therefore, to propose a robust framework for performance assessment, it is important to create test images that represent meaningful canonical cases, such as the following [50]:

- 1) homogeneous (water, bare soils, and vegetated areas);
- 2) texture;
- 3) edges (roads, rivers, and region boundaries);
- 4) isolated point target;
- 5) urban areas.

Of course, one can think of many other insightful test areas, but this is probably the smallest set of canonical images that allows one to investigate all major features of interest in SAR despeckling, that is, respectively:

- 1) speckle reduction power;
- 2) ability to tell apart speckle from texture (originated by a nonflat terrain);
- 3) preservation of contours (both location and edge profile) among different regions;
- 4) absence of radiometric distortion;
- 5) preservation of features related to man-made structures.

To collect meaningful objective indications on the performance of competing despeckling techniques we selected the following test images that consider the most common and relevant elementary scenes encountered in typical SAR images, that is, as follows:

- 1) a single flat region with constant electromagnetic parameters (Homogeneous);

- 2) a single region with constant electromagnetic parameters but nonflat orography (DEM);
- 3) several regions on flat terrain, separated by straight contours, and characterized by different electromagnetic parameters (Squares);
- 4) a corner reflector placed on a homogeneous background (Corner);
- 5) an isolated building placed on a homogeneous background (Building).

In the first four cases, the sensor parameters are those typical of the European remote sensing (ERS) or environmental satellite (ENVISAT) sensors and provide images with ground and azimuth resolution of 19.9 and 4 m, respectively. In the last case, the Cosmo/SkyMed high-resolution sensor parameters are used to ensure a resolution (3.6 m in range and 2.6 m in azimuth) adequate for the identification of a typical building. The use of a low-resolution sensor in the first four cases allows for a lower computational burden without affecting the generality of the results. In all cases, the simulator provides quite large images, corresponding to the actual extension of the imaged scene dictated by the parameters of the input sensor, ERS or ENVISAT most of the times. However, for practical reasons, we work only on small regions cropped by these images, of size 512×512 pixels for the square and DEM cases, and 256×256 pixels for the others. Moreover, although the simulator outputs SLC images, the phase content is of no interest for our applications, since despeckling algorithms typically work either on the amplitude (modulus of the complex datum) or on the intensity (square of the amplitude).

In the following, we will more thoroughly describe the five test images and will point out the major features of interest for each of them. To allow for a simple comparison among techniques, we associate with each scene/feature couple only a few (actually the most representative) numerical measures of performance. This small set of measures will help gaining a clearer insight about the potential of a given despeckling technique in different applicative scenarios, and allow establishing a meaningful comparison with competing techniques. In the following, we will motivate for each test case the proposed performance measures.

A. Homogeneous

In the first test case, we simulate the SAR image obtained in the presence of a flat surface with a constant microscopic roughness, described via an fBm process with $H = 0.75$ and $T = 0.0625$ m, and constant electromagnetic parameters $\varepsilon = 4$ and $\sigma = 0.001$ S/m. In Fig. 1, we show the first realization of the simulation (therefore, a single-look image) and the clean reference obtained by averaging all 512 realizations.

Based on this image we want to measure the speckle rejection ability of a filter. To this aim we consider a few bias indicators, that is, the mean value of the filtered image, and the mean value and variance of the ratio image and then two direct measures of performance, MSE, and ENL.

The bias indicators are useful to gain insight about the general behavior of the filter in terms of radiometric preservation

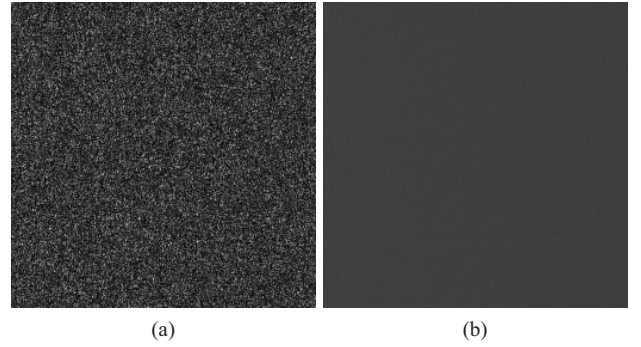


Fig. 1. Homogeneous image. (a) One-look and (b) 512-look.

and could point out its weaknesses and possible remedies. The mean value of the image (MoI), in particular, should be preserved through filtering. As for the ratio image, in principle it should contain only speckle, and hence have unit mean and variance equal $1/L$. Although small deviations from these expected values can be mostly attributed to the intrinsic variability of sample measurements, larger deviations should ring a bell. A mean of ratio (MoR) significantly different from one indicates, again, some radiometric distortion. Assuming $\text{MoR} \cong 1$, the variance of ratio (VoR) provides insight about under/oversmoothing phenomena.² A $\text{VoR} < 1$ indicates undersmoothing, that is, part of the speckle remains in the filtered image, whereas $\text{VoR} > 1$ indicates oversmoothing, that is, the filter eliminates also some details of the underlying image. Of course $\text{VoR} > 1$ makes sense only for nonflat images.

In the presence of a reference image, however, the obvious measure of choice for noise rejection is the MSE, with the statistical average replaced by sample average as follows:

$$\text{MSE}(x, \hat{x}) = \frac{1}{\text{size}(x)} \sum_{i,j} (x(i, j) - \hat{x}(i, j))^2 \quad (8)$$

where \hat{x} is the filtered image and x is the 512-look reference. To improve readability, however, we will show results on a logarithmic scale by means of the related despeckling gain measure (DG) defined here as

$$\text{DG} = 10 \log_{10} (\text{MSE}(x, z) / \text{MSE}(x, \hat{x})) \quad (9)$$

where z is the unfiltered image. Therefore, larger numbers indicate better speckle rejection. For example, a 20-dB DG indicates reduction of speckle power by a factor 100.

Together with the MSE we also report the ENL, for several good reasons: 1) it is the measure people are most used to in this field, providing immediate insight about speckle reduction ability; 2) it has a compelling physical meaning as the number of looks needed to reach the same speckle suppression level guaranteed by filtering; and 3) it can be computed also in the absence of a reference image, provided a flat region can be identified, which allows comparisons beyond the present framework. On the down side, ENL depends on the presence and detectability of a relatively large flat region of the image.

²VoR is computed as the squared error with respect to the estimated mean (MoR) and not with respect to its theoretical unitary value, as done in [38].

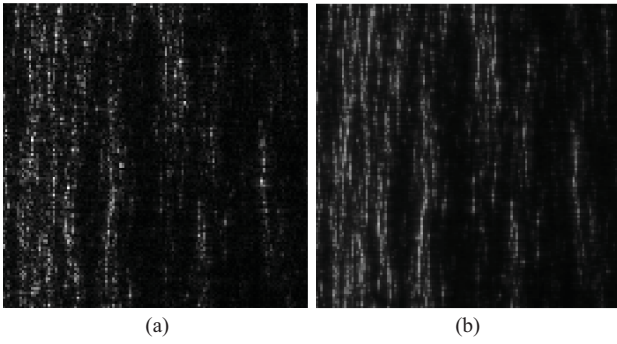


Fig. 2. DEM image. (a) One-look and (b) 512-look.

Not even our simulated scene, homogeneous by definition, has a constant mean: because of the variation of the incidence angle between near and far range, it exhibits a slight amplitude variation along the range direction, which obviously affects the ENL measures. We therefore propose a refined version of ENL, referred to as ENL^* , which removes the image amplitude variation along range, by dividing values on each fixed-range line by their average, before computing the measure. When the despeckling is very effective ENL^* can differ significantly from the conventional measure: for our clean image (512-true looks) $ENL = 437$ but $ENL^* = 510$.

B. Digital Elevation Model

In the second test case, the simulated SAR image is obtained with respect to a region with constant electromagnetic parameters $\varepsilon = 4$ and $\sigma = 0.001$ S/m and constant microscopic roughness, $H = 0.75$ and $T = 0.0625$ m, but nonflat orography. In particular, we generate an artificial canonical fractal DEM by using the Weierstrass–Mandelbrot fractal function [14] and provide it as input to the simulator. In Fig. 2, the first one-look realization and the 512-look reference image are shown whereas Fig. 3 portrays the DEM used for the simulations.

For this image, because of the presence of a macroscopic orography, some considerations about speckle generation are in order. In the previous case, the surface is macroscopically flat, implying that no significant geometrical distortion is present on the final simulated amplitude image. The considered simulator provides speckled images generating independent Rayleigh random variables and multiplying them by the amplitude value of the backscattered field evaluated in each ground range resolution cell [13]. Hence, we are assuming that the statistics for each resolution cell are those relevant to the fully developed speckle, i.e., a Rayleigh amplitude distribution. This is true also for the statistics of a homogeneous area whenever a flat surface is considered, because the change from the ground range–azimuth reference system to the slant range–azimuth one does not imply significant distortions (apart from the near-range–far-range effect). Conversely, when a significant orography is present on the imaged surface, the change in the reference system implies geometrical distortions, thus modifying the speckle statistics. The occurrence of foreshortening and layover implies that several ground range resolution cells

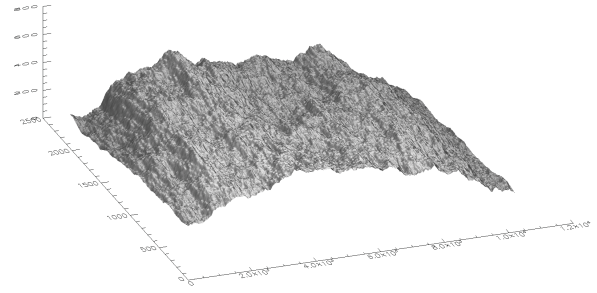


Fig. 3. Synthetic fractal DEM used for the simulations.

are mapped into one slant range resolution cell. With regard to this paper, this means that the ratio between the speckled and speckle-free intensity images generated by the SARAS simulator does not necessarily provide a Rayleigh distributed image.

Nonetheless, this case presents strong similarities with the homogeneous case discussed above, as both are uniform-terrain scenes, although with different orography. Therefore, most of the figures considered before keep making sense. The despeckling gain, in particular, remains fully informative and even more precious now, in the absence of the ENL that cannot be defined in this case. In addition, the bias indicators provide useful information although they might depart from theoretical values obtained for Rayleigh distributed speckle. In addition, we also compute the coefficient of variation $C_{\hat{x}}$, which is a widespread indicator of texture preservation. If $C_{\hat{x}}$ departs significantly from C_x the texture is certainly altered, either because of insufficient speckle rejection ($C_{\hat{x}} > C_x$) that increases the data dynamics, or because of excessive smoothing ($C_{\hat{x}} < C_x$) that reduces it. On the other hand, $C_{\hat{x}} \cong C_x$ does not guarantee the preservation of textural properties, as the coefficient of variation depends on first-order statistics only. We do not address the complex problem of texture classification, leaving it for future studies. In next section, though, we show and comment some interesting results concerning the autocovariance function (ACF) of reference and filtered images

$$ACF_x(\Delta i, \Delta j) = \frac{1}{\text{size}(x)} \sum_{i,j} [(x(i, j) - \mu_x) \times (x(i - \Delta i, j - \Delta j) - \mu_x)]. \quad (10)$$

C. Squares

In the third test case, we simulate the SAR image obtained in the presence of a flat surface, with the same microscopic roughness of the first case, but divided in four regions, with straight contours aligned to the range and azimuth coordinates, having different electromagnetic parameters. Therefore, the simulated image is made up of four areas presenting different mean intensity values. In Fig. 4, we show again the first realization together with the reference obtained by sample averaging.

Our main goal, is to assess the degradation of edges through the filtering process. To this end, we propose in this paper a new direct measure of edge smearing (ES), and use also an indirect measure, Pratt's FOM, which tells us whether the edges are still recognizable as such in the filtered image by an

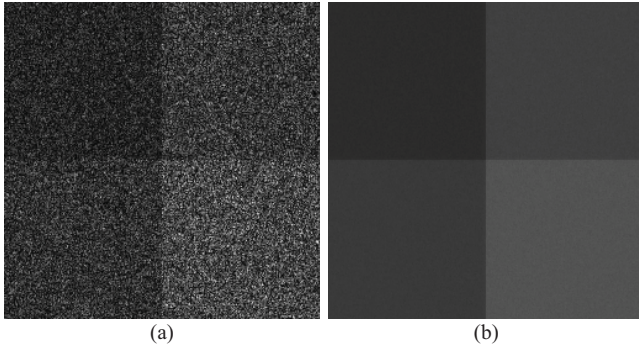


Fig. 4. Squares image. (a) One-look and (b) 512-look.

automatic detection algorithm, and hence useful for subsequent processing.

The ES, is computed as the weighted square error between the edge profiles (EPs) of the filtered and reference images

$$ES = \int g(t - t_0) (EP_{\hat{x}}(t) - EP_x(t))^2 dt \quad (11)$$

where the Gaussian kernel $g(t - t_0)$ allows us to assign a larger weight to errors that occur near the edge location t_0 . The EPs, in their turn, are computed by averaging the image in the along-edge direction over a homogeneous region, so as to obtain a virtually speckle-free signal. This is necessary to prevent the residual speckle from affecting the edge degradation measure: the original noisy image z , for example, should have a small ES figure, because no smearing occurs, even though each pixel can differ significantly from its expected value because of speckle. EPs are upsampled to obtain smoother functions and the integral is approximated by a sum.

Edge degradation can be immaterial for subsequent applications if edges can be detected anyway. Therefore, we also consider the FOM, defined [49] as follows:

$$FOM = \frac{1}{\max(n_d, n_r)} \sum_{i=1}^{n_d} \frac{1}{1 + \gamma d_i^2} \quad (12)$$

which quantifies edge-preservation by looking at the output of a suitable detection algorithm, where n_d and n_r are the number of edge pixels detected in the despeckled and reference image, respectively, d_i is the Euclidean distance between the i th detected edge pixel and the nearest reference edge pixel, and the parameter γ modulates the cost of edge displacement. Therefore, FOM penalizes both the suppression of true edges and the detection of false edges, ranging from 0 to 1, with larger values indicating superior edge rendition. In particular, we use the well-known Canny algorithm [51], selecting separately for each image the parameters (variance of the smoothing kernel and thresholds TL and TH = 4 TL) which maximize the FOM, so as to free the image quality measure from the influence of a badly tuned detection algorithm. It is worth underlining that FOM penalizes both missing edges ($n_d < n_r$) and false ones ($n_d > n_r$), as well as edges displaced with respect to their actual position ($d_i > 0$). We select $\gamma = 1/9$ so as to assign a 1/2 score to a slightly (three pixels) displaced edge. Although no theoretical proof supports the use of FOM, it is shown [52] to provide more discriminating

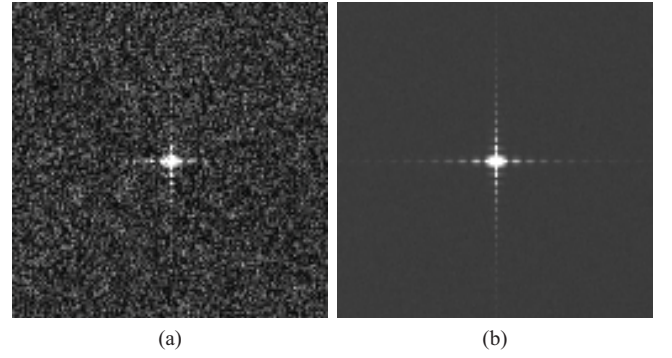


Fig. 5. Corner image. (a) One-look and (b) 512-look.

results than other measures proposed in the literature and to enable more clear-cut decisions.

D. Corner

In the fourth test case, we consider a corner reflector placed at the center of a flat homogeneous scene. We use the same setting of the first case except for the center pixel whose value is modified so as to mimic the behavior of a corner reflector. These data are then processed by the SAR simulator to provide the various realizations, the first of which is shown in Fig. 5 together with the 512-look reference.

In this case, we want to assess the radiometric preservation through the filtering process. To this end, we propose two intensity contrast measures. Let x_{CF} be the intensity observed in the corner reflector site, x_{NN} is the average intensity in the surrounding region formed by the eight-connected nearest neighbors, and x_{BG} is the average intensity of the background. Then we define

$$C_{NN} = 10 \log_{10} \frac{x_{CF}}{x_{NN}} \quad (13)$$

and

$$C_{BG} = 10 \log_{10} \frac{x_{CF}}{x_{BG}}. \quad (14)$$

In the filtered images, these figures³ should be as close as possible to the corresponding numbers computed on the reference image.

E. Building

In the last test case, we simulate the SAR image obtained in the presence of an isolated building over a homogeneous flat surface. The building is modeled as a parallelepiped with square plant of 40×40 m² and height of 20 m and is placed with one wall parallel to the line of flight of the sensor. The observed surface is modeled as a random rough surface described through the standard deviation, $\sigma_h = 0.02$ m, and the correlation length, $l_h = 0.07$ m, of the height; the building walls and rooftop are supposed to be flat and speckle-free. The same electromagnetic parameters, $\epsilon = 4$ and $\sigma = 0.001$ S/m, are used for the terrain and the building. The proposed urban simulator is able to evaluate and to correctly place on the image all the contributions arising from the interaction

³We note in passing that C_{BG} is a discrete geometry equivalent of the well-known PSLR computed when complex data are available.

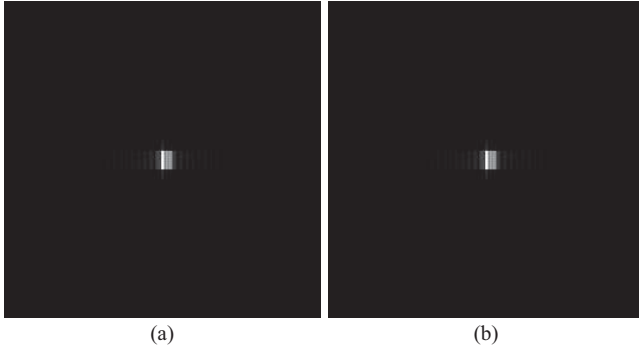


Fig. 6. Building image. (a) One-look and (b) 512-look.

between the rough terrain and the building walls. In particular, it considers double and triple reflection contributions: in case of smooth walls multiple reflection of order higher than three are not present [53]. Fig. 6 shows the first realization of the simulation together with the reference. The presence of the double reflection contribution is evident and appears as a very bright line placed at the point of intersection between the rough terrain and the building walls.

Built-up areas on high-resolution SAR images are usually very involved, presenting extreme distortion effects (layover, shadow) and, above all, many contributions related to multiple scattering mechanisms because of the presence of man-made objects on the scene under survey. Contributions associated to different buildings may overlap implying that the return from each building can mix with those relevant to neighboring structures. Thus, even if different from an actual man-made situation, the proposed case is of fundamental importance in many applications because it represents the basic element of an urban area and, more in general, of man-made structures.

Because of the presence of dihedral structures, this can be seen as a generalization of the former case to an extended man-made target. The intense double reflection line can be used to obtain estimates of the position and geometry of the observed building. In particular, the height of the building can be estimated from calibrated radiometric values of the double reflection line [54]. It is therefore important that both the position and the radiometric characteristics of the building radar return are preserved by the applied despeckling technique. Concerning radiometric precision, we compute a contrast figure

$$C_{DR} = 10 \log_{10} \frac{x_{DR}}{x_{BG}} \quad (15)$$

between the average intensity computed on the double reflection segment, x_{DR} , and the average intensity of the background x_{BG} . In addition, in analogy with the ES measure used for the square image, we propose a building smearing (BS) figure, defined as follows:

$$BS = \int \Pi \left(\frac{t - t_0}{T} \right) \left| \log_{10} (BP_{\hat{x}}(t) + \varepsilon) - \log_{10} (BP_x(t) + \varepsilon) \right| dt \quad (16)$$

with ε a small positive value, to measure the distortion of the radiometric building profile (BP) in the range direction. The BP is computed by averaging along the azimuth direction,

then we take the log to prevent the double reflection line from dominating the measure, and integrate the absolute difference with respect to the clean profile in a small range centered on the double reflection line.

V. EXPERIMENTAL RESULTS

In this section, we carry out and discuss numerical experiments using some of the despeckling techniques proposed in the literature. It is worth reminding that our goal, is not to rank these techniques in terms of performance, and possibly single out the best one, but rather to gain insight about the proposed assessment procedure and its ability to shed light on the potential and limits of each approach and algorithm. Therefore, our primary goal in the selection was to have at least one technique for each of the major approaches (spatial filtering, wavelet shrinkage, and nonlocal filtering) and possibly well-known to the community of users. Another important criterion was the availability of software code. The expected performance instead, although important, had a minor weight in the decision. In the end, we selected the following techniques and choose the parameter settings proposed in the original works.

- 1) *Kuan Filter* [19]: This is a MMSE linear adaptive filter, with multiplicative noise converted in signal-dependent additive noise, which requires the estimate of the local mean and local variance in the neighborhood (5×5) of a pixel.
- 2) *Γ -MAP Filter* [20]: This is a classification-based filter. Based on the estimated local coefficient of variation and the output of a ratio filter it decides whether to filter (with a MAP approach) the point or not, and with which local window (maximum window size is set to 11×11). Given a correct classification it preserves well the edge structure.
- 3) *Spatially Adaptive Wavelet-Based Bayesian Estimator Based on Minimum Mean Absolute Error Criterion (SAWBMMAE)* [27]: This technique works in the wavelet domain and follows the homomorphic approach assuming a Cauchy prior distribution for the coefficients of the log-transformed reflectance. The Bayesian estimation process considers also spatial dependency among wavelet coefficients by means of a linear predictive model. To reduce artifacts, the wavelet transform is implemented in the cycle-spinning mode.
- 4) *Segmentation-Based MAP Filter (MAP-S)* [28]: Speckle is modeled as a signal-dependent noise and a Bayesian MAP filter in the undecimated wavelet domain is derived assuming a generalized Gaussian prior distribution for the wavelet coefficients (to reduce artifacts, a Haar basis is used by the authors unlike in [28]). In addition, wavelet coefficients are classified according to their texture energy into several heterogeneity classes, and different models are used for each class. Strong scatterers are detected in advance and not filtered.
- 5) *Probabilistic Patch-Based Filter (PPB)* [33]: This is an extension of the NLM algorithm proposed in [31]. The Euclidean distance between patches is replaced by a more general probabilistic measure that depends

TABLE I
INFORMATION ON THE SELECTED TECHNIQUES

	References	Approach	Theory Complexity	Software
Kuan	[19]	Spatial	Low	http://www.grip.unina.it/
Γ -MAP	[20]	Spatial	Low	http://www.exelisvis.com/ProductsServices/ENVI.aspx
SAWBMMAE	[27]	Wavelet	Medium	MATLAB source code sent by the authors
MAP-S	[28]	Wavelet	Medium	experiments run by the authors
PPB	[33]	Nonlocal	High	http://www.math.u-bordeaux1.fr/~cdeledal/ppb
SAR-BM3D	[36]	Nonlocal	High	http://www.grip.unina.it/

TABLE II
MEASURES FOR HOMOGENEOUS

	MoI	MoR	VoR	ENL	ENL*	DG
Clean	1.000	0.998	0.987	436.97	510.36	—
Noisy	0.998	—	—	1.00	1.02	0
Kuan	0.998	0.971	0.732	15.95	16.42	11.91
Γ -MAP	1.023	0.959	0.824	54.00	57.80	16.64
SAWBMMAE	1.017	0.920	0.706	34.40	35.76	14.94
MAP-S	0.998	0.998	0.930	205.93	237.38	21.87
PPB	0.997	0.960	0.820	127.68	140.89	20.29
SAR-BM3D	0.978	0.979	0.814	102.44	111.91	19.40

on the noise-distribution model, and the patch-based weights are iteratively refined based on both the similarity between noisy patches and the similarity of patches extracted from the previous estimates. We use the iterative version of the algorithm (25 iterations) with a 21×21 search area and a 7×7 similarity window, and the default parameters for α and T proposed by the authors.

- 6) *SAR-BM3D* [36]: This is the SAR-oriented nonhomomorphic version of the original BM3D algorithm proposed in [32] for AWGN images. The main modifications concern the distance used in the block-matching and the local linear minimum MSE estimator used in both steps of the procedure. Parameter setting is the default one proposed in the original work.

Synthetic information about the selected algorithms is shown in Table I.

All test images are stored in intensity format and normalized to the spatial average of the corresponding clean image, which therefore has unit average intensity by definition. When visual inspection is required, we use images in amplitude format, to have a manageable dynamic, and use the same visualization scale (not just the same type of stretching) for all images of the same type. For images of different scenes or different origin, instead, we use in general different scales. All data and scripts are available for download at <http://www.grip.unina.it/>. All numbers reported in the following tables are obtained by averaging results over eight-independent single-look images of the same scene. We also computed the corresponding standard deviations. However, these are usually very small with respect to the mean, not surprisingly considering the large amount of data available in a single image, and therefore not reported in tables, for the sake of readability, but discussed in the text only in the presence of atypical behaviors.

A. Homogeneous

This is the simplest, yet most important, canonical scene, as it gives information on the speckle reduction ability of a technique.

In Table II, we report bias indicators (MoI, MoR, and VoR) and performance measures (ENL, ENL*, and DG) while in Fig. 7, we show a 256×256 -pixel section of a one-look test image, of the 512-look reference, and of the output of the despeckling filters applied to the test image. Ratio images, instead, are not much informative in this case and are not shown.

None of the filters introduces a significant bias on the mean, while only SAWBMMAE presents a biased value for the MoR. The VoR is always smaller than one, because of imperfect removal of speckle, especially for Kuan and SAWBMMAE. For this very simple scene, the bias indicators are very informative, and the performance measures confirm their indications. The best ENL, over 200, is guaranteed by MAP-S, followed by PPB, and SAR-BM3D exceeding 100, whereas the others remain much under 100. All values become a bit larger when the more accurate ENL* is considered, accounting for the near-range far-range phenomenon. In particular, the reference image has ENL* very close to the expected value of 512. As for the despeckling gain, similar considerations apply, with the best three filters providing ~ 20 dB of improvement over the noisy original. This latter measure suffers that the reference is not really clean but presents a residual variance of its own, which acts as an initial plateau for the computed MSE. For our design choices, however, this plateau is significantly smaller than the ideal MSE of the best despeckling technique.

Visual inspection allows for a subjective assessment of performance and, in addition, provides some insight on the structure of the filtered image, and especially the presence of artifacts, which are not easily captured by synthetic measures. Kuan and Γ -MAP show clearly the presence of a strong residual noise, with a significant short-range correlation because of the sliding-window filtering. SAWBMMAE and MAP-S, instead, present the footprints typical of wavelet-based techniques, much stronger and at higher frequencies in the first case, barely distinguishable in the second. Nonlocal techniques, finally, are affected by ghost artifacts, because of the attempt to recognize structures even when they are absent. This is more evident for SAR-BM3D, while PPB exhibits only some smooth brushstrokes. It seems safe to say that, in general, visual inspection confirms closely the indications given by the objective measures. However, it provides some

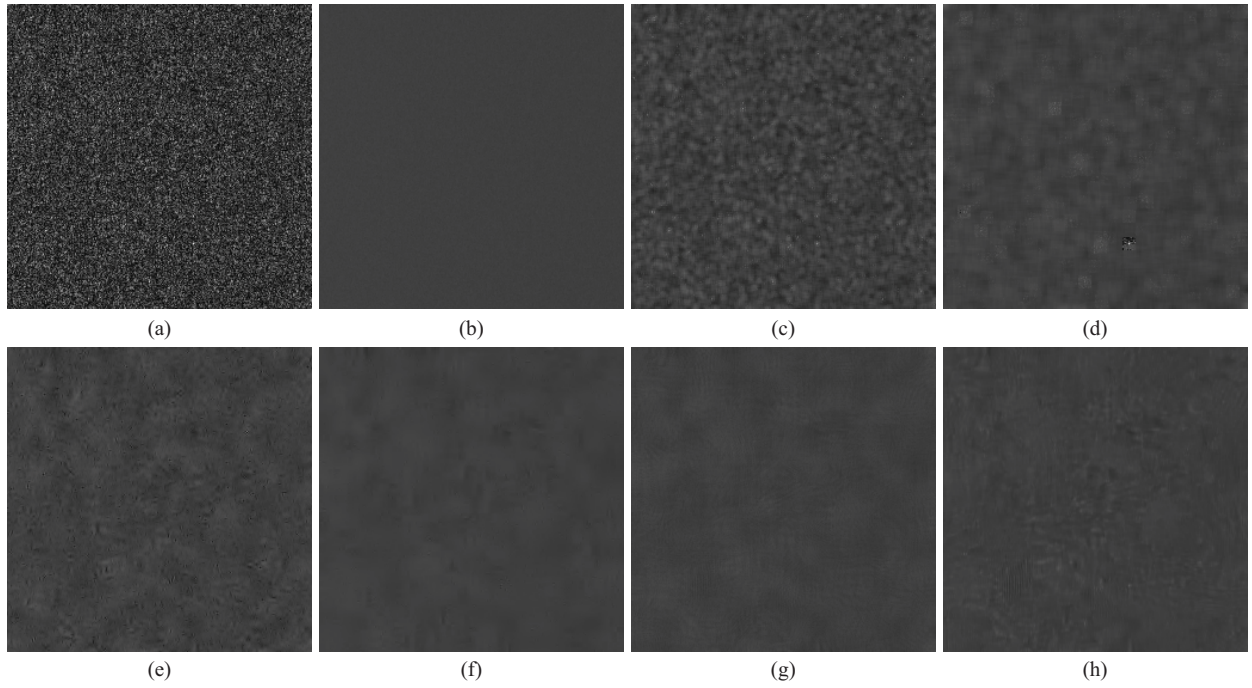


Fig. 7. Homogeneous: test, reference, and output of the six filters. (a) SAR image. (b) Clean. (c) Kuan. (d) Γ -MAP. (e) SAWBMMAE. (f) MAP-S. (g) PPB. (h) SAR-BM3D.

more information, calling for the adoption of other indicators that quantify the abundance and nuisance of artifacts generated in the filtered images. Some interesting ideas were recently proposed, in [55], where candidate artifacts are identified as off-diagonal clusters in the scatterplot of original to filtered data. We will certainly focus on this topic in future research.

B. Digital Elevation Model

This case is of great interest not only for its frequent occurrence in real-world SAR images, but also under a more abstract point of view, because the signal itself is highly textured, with a rich spectrum. Therefore, signal variations occur at different scales, some of which very short, comparable with that of the speckle. Telling apart the speckle from such high-frequency signal components is a very challenging task. In addition, just because of its random-like nature, one cannot devise a meaningful simple model of the signal, and is left basically with no tool for measuring the likely impairment of high-frequency components. In this case, therefore, more than all the others, the availability of the infinite-look version of the signal represents a precious and probably unmatched tool.

In Table III, we report the objective measures for this case, whereas Fig. 8 shows a zoom (128×128) of the test, reference, and filtered images. In addition, for the same section, we also show in Fig. 9 the ratio images. Filtered images are not significantly biased except for the SAWBBMAE case, while larger biases are observed for the ratio image. In particular, the VoR indicators for Γ -MAP and MAP-S stand out, suggesting some malfunctioning. In the first case, Γ -MAP classifies most of the image as strongly heterogeneous refraining from performing any filtering in such regions, as dictated by the algorithm. This is obvious in the ratio image which, for

TABLE III
MEASURES FOR DEM

	MoI	MoR	VoR	C_x	DG
Clean	1.000	1.001	0.999	2.40	—
Noisy	1.003	—	—	3.54	0
Kuan	0.995	0.745	0.517	1.95	4.07
Γ -MAP	1.011	0.981	0.033	3.48	0.08
SAWBMMAE	0.781	0.914	0.929	2.14	4.75
MAP-S	1.004	2.404	7933	3.35	0.31
PPB	0.998	0.911	0.560	2.71	3.68
SAR-BM3D	0.968	0.833	0.415	2.43	5.32

Γ -MAP, is mostly constant, hence $\text{VoR} \approx 0$. This problem appears to be intrinsic of the algorithm, and can be solved only with the use of a better classifier. The wavelet-based MAP-S, instead, happens to produce some negative values after filtering (clipped to the machine ε) because of the oscillating basis functions. We keep the output as is, but the problem in this case could be easily solved by a smarter form of clipping or through the use of robust statistics. Even barring these pathological cases, most techniques present small values of VoR, which testifies their inability to fully reject speckle in this challenging situation. On the other hand, even a unitary value does not guarantee good despeckling, as the VoR is influenced also by the unwanted filtering of signal component. For this image, therefore, the despeckling gain is definitely more informative. The best performance is provided by SAR-BM3D, over 5 dB (but compare it with the 20 dB of the homogeneous case), with SAWBMMAE just under 5 dB and the others further back. In terms of coefficient of variation, SAR-BM3D is again the best, with a value of 2.43, very close to the 2.40 of the 512-look image.

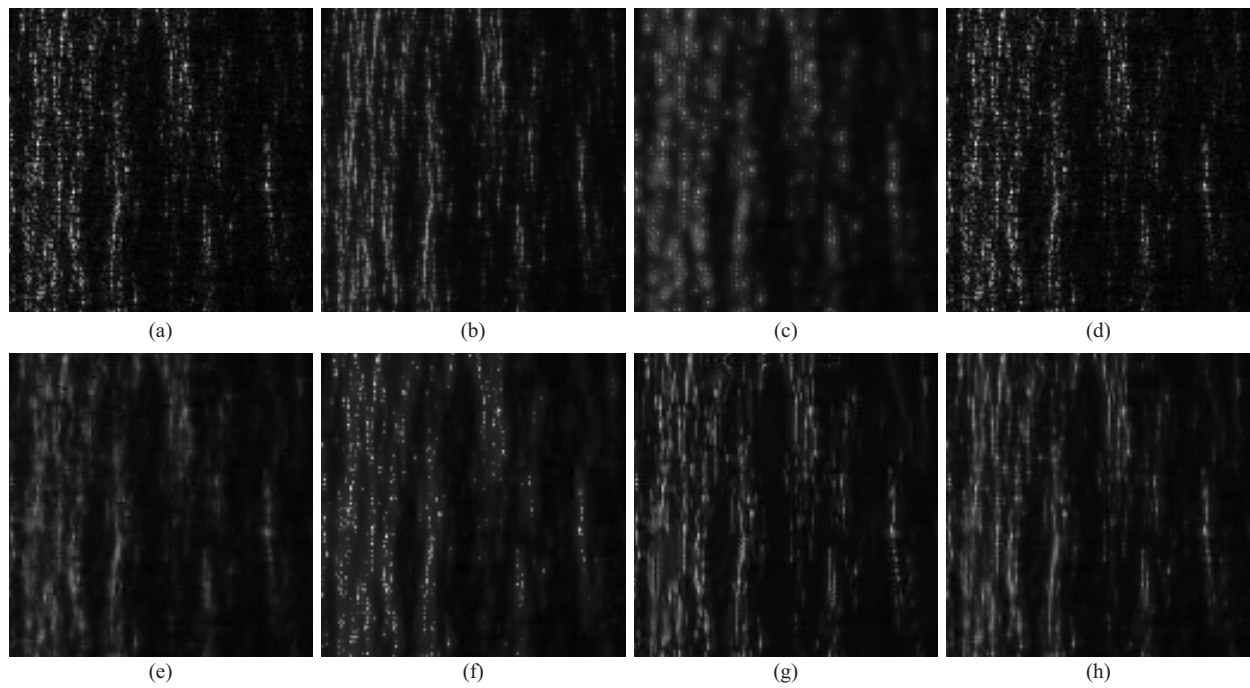


Fig. 8. DEM: test, reference, and output of the six filters. (a) SAR image. (b) Clean. (c) Kuan. (d) Γ -MAP. (e) SAWBMMAE. (f) MAP-S. (g) PPB. (h) SAR-BM3D.

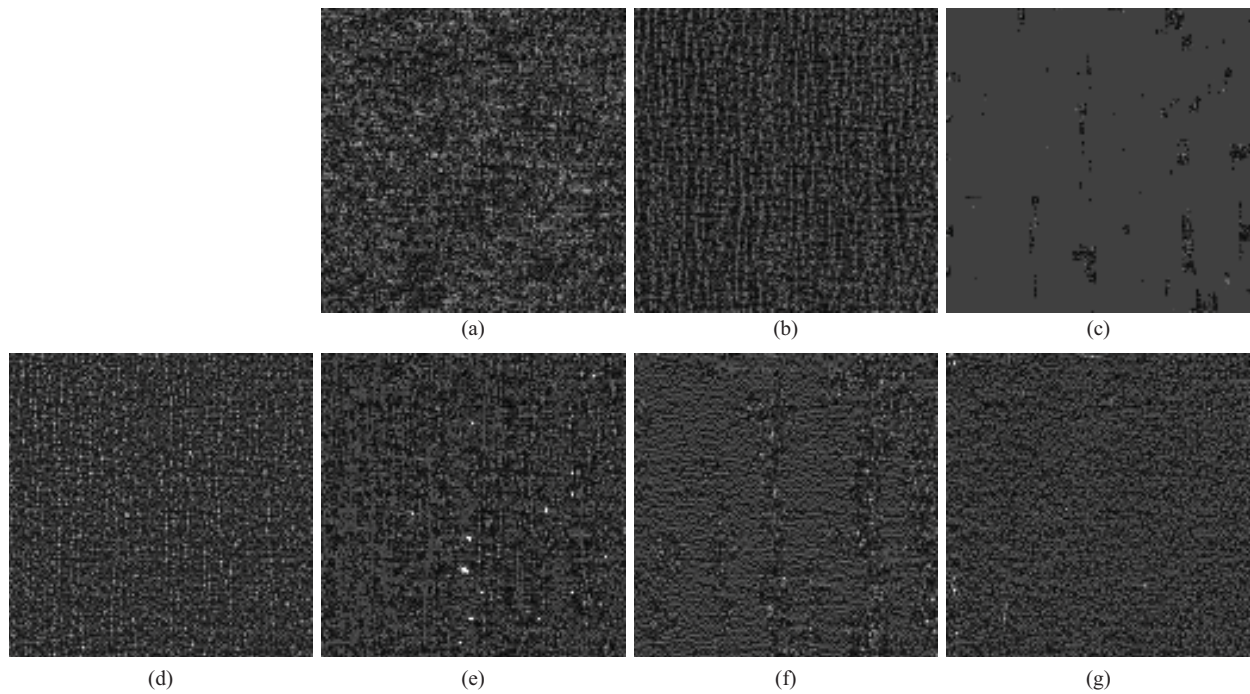


Fig. 9. DEM: ratio images for the reference and the six filters. (a) Clean. (b) Kuan. (c) Γ -MAP. (d) SAWBMMAE. (e) MAP-S. (f) PPB. (g) SAR-BM3D.

In this case, the visual inspection of ratio images is especially insightful, as these clearly show traces of signal-related structures, proving that part of the signal is filtered away. Leaving aside the pathological case of Γ -MAP, vertical structures are recognizable in all ratio images, with the notable exception of SAR-BM3D.

Concerning the preservation of structural properties of the image, it is worth analyzing briefly the behavior of the ACF along the range direction, reported for all images in Fig. 10.

Preserving its shape can be reasonably considered as a basic condition for texture preservation. On the other hand, the ACF provides valuable information by itself on the underlying texture, even allowing the accurate estimation of the fractal dimension of the imaged natural surface, as recently shown in [56] and [57]. Fig. 10 shows clearly that, for almost all filtered images, the ACF behaves like that of the clean image at large spatial scales, while it becomes markedly different at shorter scales, where textural properties can be therefore

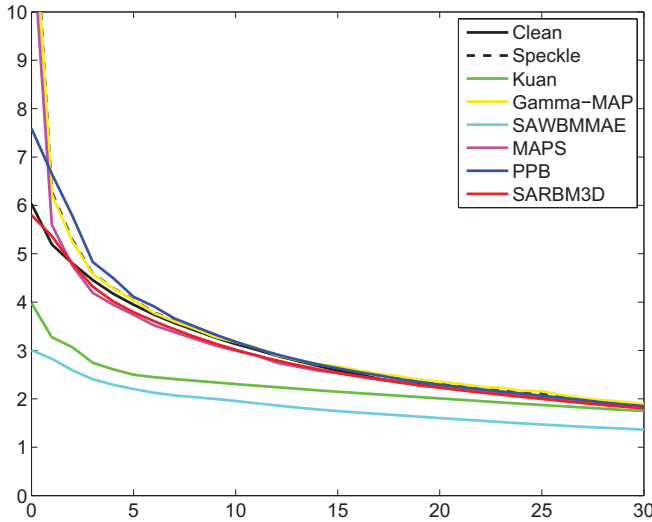


Fig. 10. DEM: mean ACF along the range direction for test, reference, and the six filters.

expected to differ significantly from those of the clean image. The extent of the range of scales where the ACF of the filtered image fits that of the clean reference makes therefore an interesting candidate for a synthetic index of structure preservation. However, to define such an index, a deeper analysis is necessary that goes beyond the scope of this paper, and we leave it to future work.

C. Squares

In Table IV, we report the ES figures for the two vertical edges, characterized by lower (up) and higher (down) contrast, together with the FOM for the detected edges. Fig. 11 shows the test, reference, and filtered images. Visual inspection tells us that, to avoid edge blurring, the best we can do is to avoid filtering altogether. All filtered images, exhibit edge smearing, in varying degree, particularly annoying for Γ -MAP that exercises the strongest smoothing. This impression is confirmed by looking at the profiles of the upper edge, plotted in Fig. 12. For the sake of clarity, we plot EPs separately for each filtered image, with six-times oversampling and spline interpolation, reporting each time the 512-look image EP as a reference. Because of the point-spread function of the system, the latter is not a simple step edge. In this case, the sharpest edges are provided by Kuan, which carries out a lighter filtering, and SAR-BM3D through the nonlocal approach. This is obviously confirmed by the ES figures, which are different for the up and down edges because of the different contrast, but provide consistently the same ranking of filters. It must be pointed out, however, that the ES measures present a significant standard deviation over the eight test images, up to 1/3 of the mean value, because of the limited data available, consisting of the few lines along the edges. As such, they are somewhat less reliable than other indicators.

Of course, ES provides only part of the information of interest. It does not say whether the edge will be ultimately recognized as such, and in the right position, by a detector, nor it considers false edges originated by unfiltered speckle

TABLE IV
MEASURES FOR SQUARES

	ES (up)	ES (down)	FOM
Clean			0.993
Noisy	0.010	0.029	0.792
Kuan	0.043	0.118	0.797
Γ -MAP	0.118	0.297	0.825
SAWBMMAE	0.079	0.211	0.770
MAP-S	0.062	0.187	0.868
PPB	0.070	0.209	0.837
SAR-BM3D	0.036	0.113	0.847

or by filtering artifacts. If we look at the output of the Canny edge detector, in Fig. 13, it is clear that no image guarantees a perfect edge rendition. The edges are never perfectly straight and in some cases, markedly for the linear filters and SAWBMMAE, large parts of the low-contrast horizontal edges are missed toward the center of the image. This phenomenon, caused by the presence of stronger edges nearby, is less severe for the other techniques. This empirical ranking is well-captured by the FOM, as MAP-S provides the best numerical result, 0.868 on the average (standard deviations are always negligible) followed closely by the nonlocal techniques and Γ -MAP. Kuan is ineffective and SAWBMMAE even detrimental, with a FOM of 0.770 against 0.792 for the noisy images. It is worth remembering, however, that, to decouple the potential edge information conveyed by each image from the specific edge detector details, we select for each single image the Canny parameters that maximize the FOM (which is also why we never observe false edges). In particular, the Canny detector includes a Gaussian low-pass filter that sort of equalizes the performance of different filters. The selected σ parameter is over 20 (strong filtering) for noisy, Kuan, Γ -MAP, and SAWBMMAE and <10 (light filtering) for the others.

D. Corner

This situation occurs in SAR images for the presence of artificial corner reflectors used in the framework of measurement campaigns and, much more frequently, because trihedral structures of appropriate dimension act as corner reflectors, implying high intensity returns on the images. This phenomenon is much more evident in very high-resolution images, where also trihedral structures of small size can act as corner reflectors. In this case, a good despeckling technique should not significantly modify the corner reflector response: both the contrast of the corner main lobe with respect to the background intensity value and the contrast with regard to the nearest neighboring pixels are of interest for calibration and image registration purposes. Hence, as in Section IV-D, in this case, the measures of interest are aimed at evaluating radiometric preservation.

In Table V, we report the contrast values C_{NN} and C_{BG} , whereas Fig. 14 shows a zoom (128×128) of the test, reference, and filtered images. In this case, as already said for edge preservation, the best strategy is to avoid any filtering in the easily detected corner reflector region (see contrast values for the noisy image). Γ -MAP and MAP-S both follow

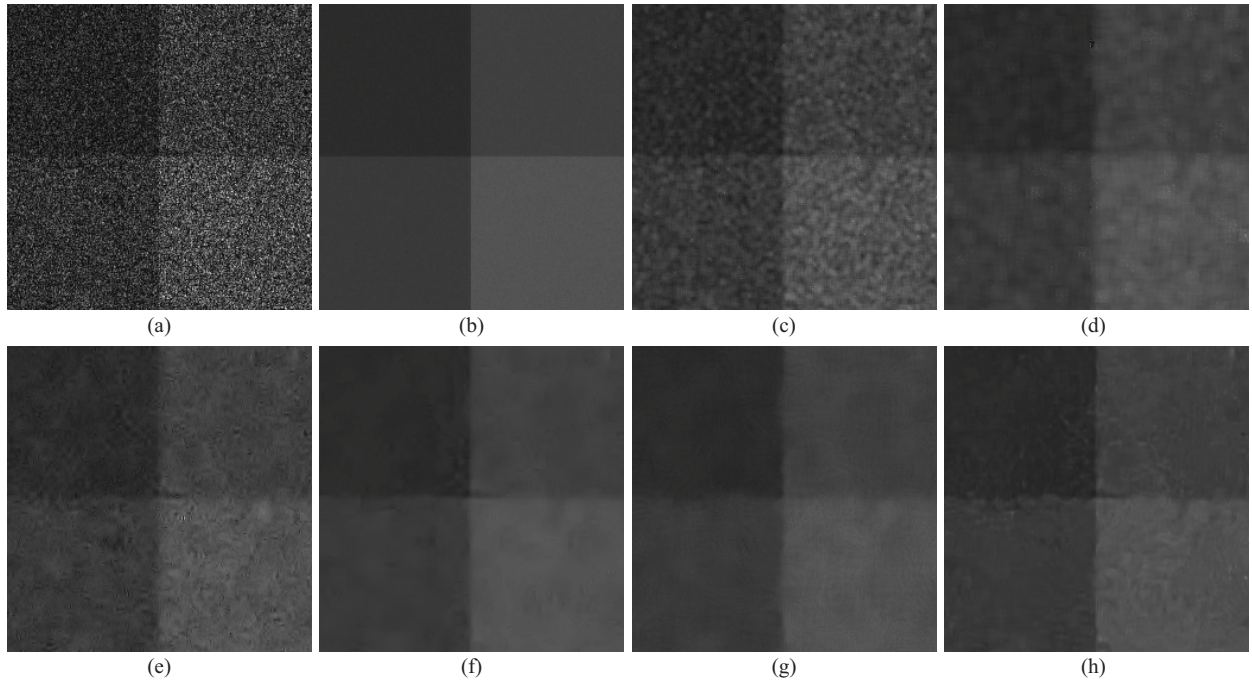


Fig. 11. Squares: test, reference, and output of the six filters. (a) SAR image. (b) Clean. (c) Kuan. (d) Γ -MAP. (e) SAWBMMAE. (f) MAP-S. (g) PPB. (h) SAR-BM3D.

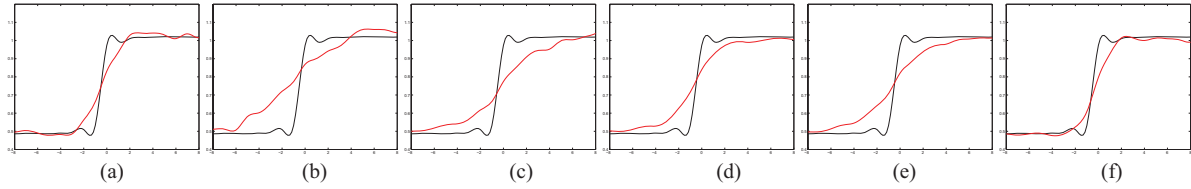


Fig. 12. Squares: EPs (upper edge) obtained for the six filters (red) compared with the clean one (black). (a) Kuan. (b) Γ -MAP. (c) SAWBMMAE. (d) MAP-S. (e) PPB. (f) SAR-BM3D.

TABLE V
MEASURES FOR CORNER

	C_{NN}	C_{BG}
Clean	7.75	36.56
Noisy	7.77	36.50
Kuan	6.36	33.35
Γ -MAP	7.77	36.39
SAWBMMAE	3.13	21.86
MAP-S	7.80	36.50
PPB	3.75	32.69
SAR-BM3D	7.39	35.45

TABLE VI
MEASURES FOR BUILDING

	C_{DR}	BS
Clean	65.90	
Noisy	65.90	0.09
Kuan	62.82	15.59
Γ -MAP	65.79	6.35
SAWBMMAE	64.24	7.38
MAP-S	65.90	0.30
PPB	64.90	3.13
SAR-BM3D	65.91	1.46

this strategy, although in different ways, obtaining very good contrast indicators and preserving fairly well the shape of the point target response, as shown in Fig. 15, where a range profile of the corner response is presented. On the other hand, they both produce visible artifacts in the output image because of the sharp transition between the filtered and nonfiltered regions. Among the other techniques, not based on prior classification, SAR-BM3D provides good results in terms of both numerical indicators and visual quality, with no annoying artifacts, Kuan and PPB appear to be still acceptable, despite an appreciable loss in contrast, while SAWBMMAE

is certainly inadequate as it strongly affects the radiometric properties of the corner signature, giving rise to a severe smoothing effect easily appreciated in Figs. 14(e) and 15(c).

E. Building

In Fig. 16, a zoom (128×128) of the ratio image for the test, reference, and filtered images is presented, whereas Table VI provides the C_{DR} and the BS values defined in (15) and (16), respectively. Almost all techniques preserve the double reflection line quite accurately, either because of prior classification or through an effective feature-preserving

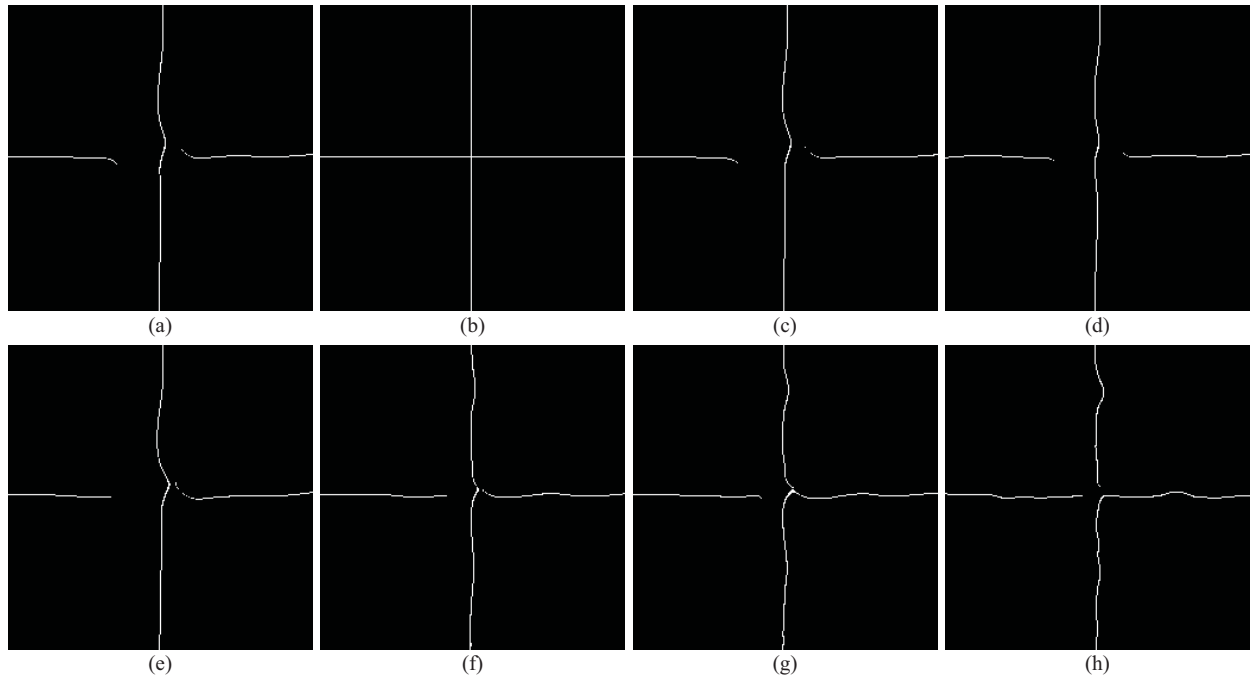


Fig. 13. Squares: edge maps for test, reference, and the six filters. (a) SAR image. (b) Clean. (c) Kuan. (d) Γ -MAP. (e) SAWBMMAE. (f) MAP-S. (g) PPB. (h) SAR-BM3D.

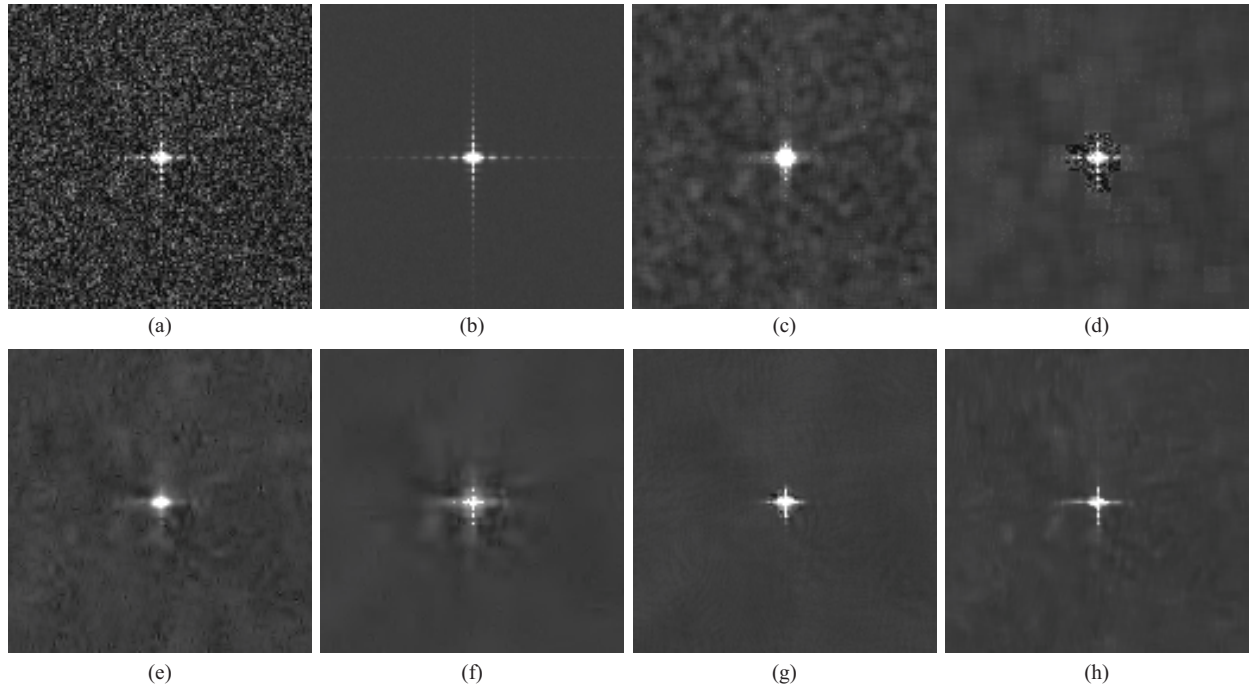


Fig. 14. Corner reflector: test, reference, and output of the six filters. (a) SAR image. (b) Clean. (c) Kuan. (d) Γ -MAP. (e) SAWBMMAE. (f) MAP-S. (g) PPB. (h) SAR-BM3D.

filtering, the only exception being Kuan, which loses >3 dB in the contrast indicator. The BS measure points out more significant differences as it considers the whole building profile. Such different behaviors can be also visually appreciated by looking at Fig. 17, where average range profiles (obtained averaging over the range lines interested by the presence of the building) are shown in logarithmic scale, in red for the filtered

images and in black for the reference (512-look). In particular, while MAP-S identifies correctly the whole building region and preserves it integrally, with BS very close to zero, Γ -MAP fails to recognize the long-range effects of the building on the image, smoothing the low-contrast lobes to the left of it, as testified by the much larger smearing indicator, $BS = 6.35$. SAR-BM3D and PPB also perform very well, despite the lack

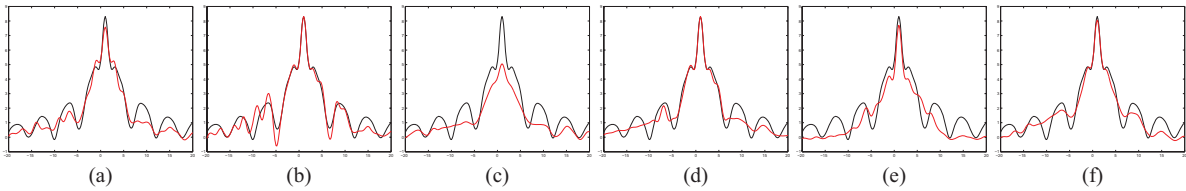


Fig. 15. Corner reflector: range profiles obtained for the six filters (red) compared with the clean one (black). (a) Kuan. (b) Γ -MAP. (c) SAWBMMAE. (d) MAP-S. (e) PPB. (f) SAR-BM3D.

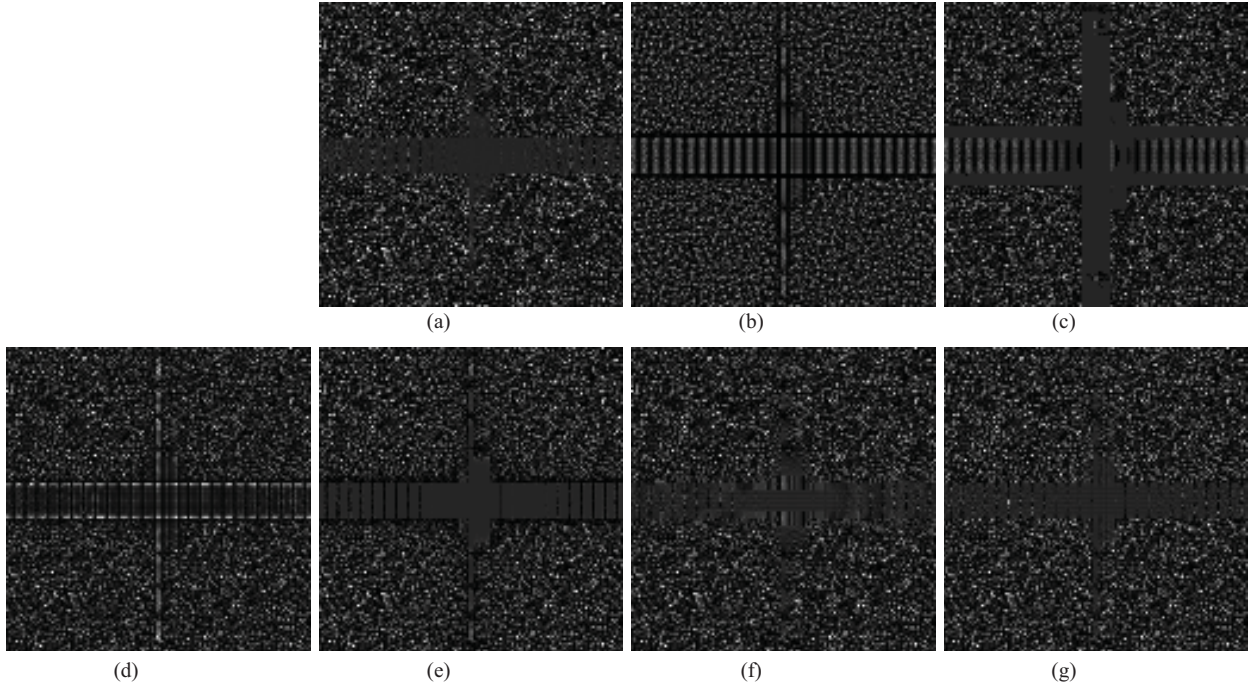


Fig. 16. Building: ratio images for the reference and the six filters. (a) Clean. (b) Kuan. (c) Γ -MAP. (d) SAWBMMAE. (e) MAP-S. (f) PPB. (g) SAR-BM3D.

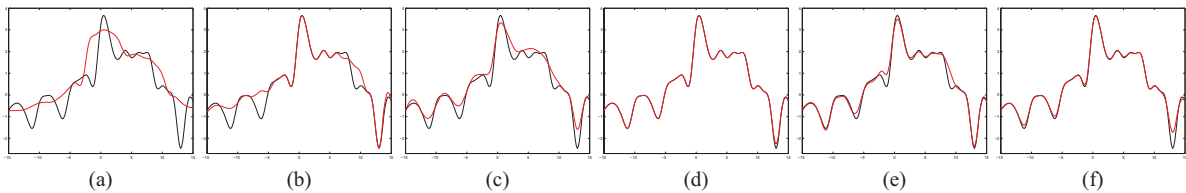


Fig. 17. Building profiles: range profiles obtained for the six filters (red) compared with the clean one (black). (a) Kuan. (b) Γ -MAP. (c) SAWBMMAE. (d) MAP-S. (e) PPB. (f) SAR-BM3D.

of a prior classification, while SAWBMMAE and especially Kuan tend to smooth the signal pattern related to the presence of the building. It is worth underlining that these, or similar, profiles can be used to retrieve physical information on the observed building by means of pattern recognition algorithms, see [58]. The BS measure is therefore an effective index of the preservation of the characteristic building pattern on the SAR image.

The visual inspection of the ratio images in Fig. 16 confirms the above consideration, with regular pattern appearing where the filtering smears the building profile.

VI. CONCLUSION

SAR despeckling draws an ever increasing attention in the scientific literature, with several new techniques proposed each

year. Currently, however, performance assessment is carried out either by visual inspection on proprietary SAR images or by using optical images with simulated speckle, both unsatisfactory tools for different reasons. The absence of established benchmarking tools leaves researchers and practitioners alike with little clues on the actual performance of techniques, and represents a major obstacle to progress in this field, preventing a healthy competition of ideas.

To fill this gap, in this paper, we proposed a new paradigm for the assessment of SAR despeckling techniques, based on physical-level SAR image simulation. This approach allowed us to obtain objective and fully replicable results on canonical scenes that, in the limits of the simulation model can be considered as the realistic output of a SAR system. The opportunity to generate repeated instances of the same scene

provided us with true full-resolution multilook images with an arbitrary number of looks, and hence with a fully reliable and meaningful reference image for each scene.

After outlining the general approach, we also proposed a practical implementation of it by selecting a set of canonical scenes that covered most of the typical cases occurring in SAR imagery, and a corresponding set of performance measures, some well-known, some proposed for the first time in this paper, that capture in numbers the behavior of a given technique in terms of speckle suppression and feature-preservation ability.

Finally, to gain insight about the actual potential of this tool we also selected a set of representative despeckling algorithms, including some of the most widespread and well-understood in the user community, and conducted sample numerical experiments, comparing numerical results with the information gathered by the visual inspection of images. Early results were extremely encouraging: the indications given by numerical measures were always fully consistent with the rationale specific of each considered despeckling technique, strongly agree with qualitative (expert) visual inspections, and provide insight into SAR despeckling approaches.

The proposed set of images and norms, available to the interested community (<http://grip.unina.it>), can be considered as the first nucleus of a complete benchmarking tool that will allow researchers and practitioners to test and compare existing techniques, and to develop and fine-tune new ones.

Nonetheless, we are well aware that most of the research on this topic is still ahead, further investigation is needed, and a number of critical decisions must be made before trying to define an actual benchmark for despeckling techniques based on this approach. Indeed, the choices made in this paper, although maybe reasonable, can be considered only as a starting point for the definition of a more thorough assessment protocol, and a number of questions must be first addressed: what canonical scenes should be selected to enable a comprehensive study of performance? And what numerical measures better account for the different behavior of techniques? How can one objectively consider the artifacts introduced with different approaches? Is it possible to define an overall index of performance, or more likely one specific index for each application, which provides a meaningful ranking of competing techniques? We are certainly bound to explore some of these topics in near future, but it became increasingly clear to us, as this research proceeded, that most of the answers to these questions should come from a broad consensus of opinion in the scientific community, and we hope that other research groups and interested parties will indeed contribute to this effort.

On the other hand, this large number of open issues is the direct consequence of the many degrees of freedom allowed by this approach. The proposed physical simulation enables the generation of SAR images and corresponding speckle free counterparts for any choice of the scene (dielectric constants, dimensions of the objects, contrast between objects, and background) and sensor parameters (wavelength, resolution, and operational mode). Therefore it provides the methodology to define and implement not just one, but any sort of benchmark,

as suggested by the title of this paper, that might be deemed useful to test present and future SAR despeckling techniques.

REFERENCES

- [1] G. Di Martino, M. Poderico, G. Poggi, D. Riccio, and L. Verdoliva, "SAR image simulation for the assessment of despeckling techniques," in *Proc. IEEE Int. Geosci. Remote Sens. Symp.*, Jul. 2012, pp. 1797–1800.
- [2] J. M. Durand, B. J. Gimonet, and J. R. Perbos, "SAR data filtering for classification," *IEEE Trans. Geosci. Remote Sens.*, vol. 25, no. 5, pp. 629–637, Sep. 1987.
- [3] Z. Zeng and I. G. Cumming, "SAR image data compression using a tree-structured wavelet transform," *IEEE Trans. Geosci. Remote Sens.*, vol. 39, no. 3, pp. 546–552, Mar. 2001.
- [4] E. Bratsolis and M. Sigelle, "Fast SAR image restoration, segmentation, and detection of high-reflectance regions," *IEEE Trans. Geosci. Remote Sens.*, vol. 41, no. 12, pp. 2890–2899, Dec. 2003.
- [5] D. Espinoza Molina, D. Gleich, and M. Datcu, "Evaluation of bayesian despeckling and texture extraction methods based on Gauss-Markov and auto-binomial gibbs random fields: Application to TerraSAR-X Data," *IEEE Trans. Geosci. Remote Sens.*, vol. 50, no. 5, pp. 2001–2025, May 2012.
- [6] E. Trouvé, Y. Chambenoit, N. Classeau, and P. Bolon, "Statistical and operational performance assessment of multitemporal SAR image filtering," *IEEE Trans. Geosci. Remote Sens.*, vol. 41, no. 11, pp. 2519–2530, Nov. 2003.
- [7] L. Gomez, C. Munteanu, J. Jacobo-Berlles, and M. Mejail, "Evolutionary expert-supervised despeckled SRAD filter design for enhancing SAR images," *IEEE. Geosci. Remote Sens. Lett.*, vol. 8, no. 4, pp. 814–818, Jun. 2011.
- [8] Y. Sheng and Z. Xia, "A comprehensive evaluation of filters for radar speckle suppression," in *Proc. IEEE Int. Geosci. Remote Sens. Symp.*, vol. 3, May 1996, pp. 1559–1561.
- [9] Y. Dong, A. K. Milne, and B. C. Forster, "A review of SAR speckle filters: Texture restoration and preservation," in *Proc. IEEE Int. Geosci. Remote Sens. Symp.*, vol. 2, Jul. 2000, pp. 633–635.
- [10] Y. Yan, Y. Zhou, and C. Li, "Quantitative assessment of speckle filters for SAR images," *Proc. SPIE*, vol. 4875, pp. 428–433, Jul. 2002.
- [11] J. W. Goodman, "Some fundamental properties of speckle," *J. Opt. Soc. Am.*, vol. 66, no. 11, pp. 806–814, Nov. 1976.
- [12] F. T. Ulaby and M. C. Dobson, *Handbook of Radar Scattering: Statistics for Terrain*. Norwood, MA, USA: Artech House, 1989.
- [13] G. Franceschetti, M. Migliaccio, D. Riccio, and G. Schirrinzi, "SARAS: A SAR raw signal simulator," *IEEE Trans. Geosci. Remote Sens.*, vol. 30, no. 1, pp. 110–123, Jan. 1992.
- [14] G. Franceschetti and D. Riccio, *Scattering, Natural Surfaces and Fractals*. Burlington, MA, USA: Academic, 2007.
- [15] G. Franceschetti, A. Iodice, and D. Riccio, "A canonical problem in electromagnetic backscattering from buildings," *IEEE Trans. Geosci. Remote Sens.*, vol. 40, no. 8, pp. 1787–1801, Aug. 2002.
- [16] R. K. Raney and G. J. Wessels, "Spatial considerations in SAR speckle simulation," *IEEE Trans. Geosci. Remote Sens.*, vol. 26, no. 5, pp. 666–672, Sep. 1988.
- [17] J. S. Lee, "Speckle analysis and smoothing of synthetic aperture radar images," *Comput. Graph. Image Process.*, vol. 17, no. 1, pp. 24–32, Sep. 1981.
- [18] V. S. Frost, J. A. Stiles, K. S. Shanmugan, and J. C. Holtzmann, "A model for radar images and its application to adaptive digital filtering of multiplicative noise," *IEEE Trans. Pattern Anal. Mach. Intell.*, vol. 4, no. 2, pp. 157–166, Mar. 1982.
- [19] D. T. Kuan, A. A. Sawchuk, T. C. Strand, and P. Chavel, "Adaptive noise smoothing filter for images with signal-dependent noise," *IEEE Trans. Pattern Anal. Mach. Intell.*, vol. 7, no. 2, pp. 165–177, Mar. 1985.
- [20] A. Lopes, E. Nezry, R. Touzi, and H. Laur, "Structure detection and statistical adaptive speckle filtering in SAR images," *Int. J. Remote Sens.*, vol. 14, no. 9, pp. 1735–1758, 1993.
- [21] Y. Yu and S. T. Acton, "Speckle reducing anisotropic diffusion," *IEEE Trans. Image Process.*, vol. 11, no. 11, pp. 1260–1270, Nov. 2002.
- [22] J. M. Nicolas, F. Tupin, and H. Maitre, "Smoothing speckled SAR images by using maximum homogeneous region filters: An improved approach," in *Proc. IEEE Int. Geosci. Remote Sens. Symp.*, vol. 3, Jul. 2001, pp. 1503–1505.
- [23] H. Feng, B. Hou, and M. Gong, "SAR image despeckling based on local homogeneous-region segmentation by using pixel-relativity measurement," *IEEE Trans. Geosci. Remote Sens.*, vol. 49, no. 7, pp. 2724–2737, Jul. 2011.

- [24] H. Guo, J. Odegard, M. Lang, R. Gopinath, I. Selesnick, and C. Burrus, "Wavelet based speckle reduction with application to SAR based ATDR," in *Proc. IEEE Int. Conf. Image Process.*, vol. 1, Jan. 1994, pp. 75–79.
- [25] L. Gagnon, "Speckle filtering of SAR images: A comparative study between complex wavelet-based and standard filters," *Proc. SPIE*, vol. 3169, pp. 80–91, Oct. 1997.
- [26] A. Achim, E. E. Kuruoglu, and J. Zerubia, "SAR image filtering based on the heavy-tailed Rayleigh model," *IEEE Trans. Image Process.*, vol. 15, no. 9, pp. 2686–2693, Sep. 2006.
- [27] M. I. H. Bhuiyan, M. O. Ahmad, and M. N. S. Swamy, "Spatially adaptive wavelet-based method using the Cauchy prior for denoising the SAR images," *IEEE Trans. Circuits Syst. Video Technol.*, vol. 17, no. 4, pp. 500–507, Apr. 2007.
- [28] T. Bianchi, F. Argenti, and L. Alparone, "Segmentation-based MAP despeckling of SAR images in the undecimated wavelet Domain," *IEEE Trans. Geosci. Remote Sens.*, vol. 46, no. 9, pp. 2728–2742, Sep. 2008.
- [29] J. J. Ranjani and S. J. Thiruvengadam, "Generalized SAR despeckling based on DTCWT exploiting interscale and intrascale dependences," *IEEE Geosci. Remote Sens. Lett.*, vol. 8, no. 3, pp. 552–556, May 2011.
- [30] F. Argenti, T. Bianchi, A. Lapini, and L. Alparone, "Fast MAP despeckling based on laplacian-gaussian modeling of wavelet coefficients," *IEEE Geosci. Remote Sens. Lett.*, vol. 9, no. 1, pp. 13–17, Jan. 2012.
- [31] A. Buades, B. Coll, and J. M. Morel, "A review of image denoising algorithms, with a new one," *Multiscale Model. Simul.*, vol. 4, no. 2, pp. 490–530, 2005.
- [32] K. Dabov, A. Foi, V. Katkovnik, and K. Egiazarian, "Image denoising by sparse 3-D transform-domain collaborative filtering," *IEEE Trans. Image Process.*, vol. 16, no. 8, pp. 2080–2095, Aug. 2007.
- [33] C. A. Deledalle, L. Denis, and F. Tupin, "Iterative weighted maximum likelihood denoising with probabilistic patch-based weights," *IEEE Trans. Image Process.*, vol. 18, no. 12, pp. 2661–2672, Dec. 2009.
- [34] M. Makitalo, A. Foi, D. Fevrale, and V. Lukin, "Denoising of single-look SAR images based on variance stabilization and nonlocal filters," in *Proc. Int. Conf. Math. Methods Electromagn. Theory*, Sep. 2010, pp. 1–4.
- [35] H. Zhong, Y. Li, and L. C. Jiao, "SAR image despeckling using Bayesian nonlocal means filter with sigma preselection," *IEEE Geosci. Remote Sens. Lett.*, vol. 8, no. 4, pp. 809–813, Jul. 2011.
- [36] S. Parrilli, M. Poderico, C. V. Angelino, and L. Verdoliva, "A nonlocal SAR image denoising algorithm based on LMMSE wavelet shrinkage," *IEEE Trans. Geosci. Remote Sens.*, vol. 50, no. 2, pp. 606–616, Feb. 2012.
- [37] D. Cozzolino, S. Parrilli, G. Scarpa, G. Poggi, and L. Verdoliva, "Fast adaptive nonlocal SAR despeckling," *IEEE Geosci. Remote Sens. Lett.*, 2013 to be published.
- [38] C. Oliver and S. Quegan, *Understanding Synthetic Aperture Radar Images*. Raleigh, NC, USA: SciTech, 2004.
- [39] S. Solbo and T. Eltoft, "Homomorphic wavelet-based statistical despeckling of SAR images," *IEEE Trans. Geosci. Remote Sens.*, vol. 42, no. 4, pp. 711–721, Apr. 2004.
- [40] R. Touzi, "A review of speckle filtering in the context of estimation theory," *IEEE Trans. Geosci. Remote Sens.*, vol. 40, no. 11, pp. 2392–2404, Nov. 2002.
- [41] F. T. Ulaby, F. Kouyate, B. Brisco, and T. Williams, "Textural information in SAR images," *IEEE Trans. Geosci. Remote Sens.*, vol. GE-24, no. 2, pp. 235–245, Jan. 1986.
- [42] M. Walessa and M. Datcu, "Model-based despeckling and information extraction from SAR images," *IEEE Trans. Geosci. Remote Sens.*, vol. 38, no. 5, pp. 2258–2269, Sep. 2000.
- [43] Z. Wang, A. C. Bovik, H. R. Sheikh, and E. P. Simoncelli, "Image quality assessment: From error visibility to structural similarity," *IEEE Trans. Image Process.*, vol. 13, no. 4, pp. 600–612, Apr. 2004.
- [44] J. S. Lee, I. Jurkevich, P. Dewaele, P. Wambacq, and A. Oosterlinck, "Speckle filtering of synthetic aperture radar images: A review," *Remote Sens. Rev.*, vol. 8, no. 4, pp. 313–340, Jan. 1994.
- [45] F. Sattar, L. Florey, G. Salomonsson, and B. Lovstrom, "Image enhancement based on a nonlinear multiscale method," *IEEE Trans. Image Process.*, vol. 6, no. 6, pp. 888–95, Jan. 1997.
- [46] Y. Dong, A. K. Milne, and B. C. Forster, "Toward edge sharpening: A SAR speckle filtering algorithm," *IEEE Trans. Geosci. Remote Sens.*, vol. 39, no. 4, pp. 851–863, Apr. 2001.
- [47] G. Franceschetti, V. Pascasio, and G. Schirrinzi, "Iterative homomorphic technique for speckle reduction in synthetic-aperture radar imaging," *J. Opt. Soc. Amer. A*, vol. 12, no. 4, pp. 686–694, Apr. 1995.
- [48] J. M. Park, W. J. Song, and W. A. Pearlman, "Speckle filtering of SAR images based on adaptive windowing," *IEEE Proc. Vis. Image Signal Process.*, vol. 146, no. 4, pp. 191–197, Aug. 1999.
- [49] W. K. Pratt, *Digital Image Processing*. New York, NY, USA: Interscience, 1978.
- [50] E. Nezry, A. Lopes, and R. Touzi, "Detection of structural and textural features for SAR images filtering," in *Proc. IEEE Int. Geosci. Remote Sens. Symp. Remote Sensing, Global Monitor. Earth Manage.*, vol. 4, Jun. 1991, pp. 2169–2172.
- [51] J. Canny, "A computational approach to edge detection," *IEEE Trans. Pattern Anal. Machine Intell.*, vol. 8, no. 6, pp. 679–698, Nov. 1986.
- [52] S. Chabrier, H. Lauren, C. Rosenberger, and B. Emile, "Comparative study of contour detection evaluation criteria based on dissimilarity measures," *J. Image Video Process.*, vol. 2008, no. 2, pp. 1–13, 2008.
- [53] G. Franceschetti, A. Iodice, D. Riccio, and G. Ruello, "SAR raw signal simulation for urban structures," *IEEE Trans. Geosci. Remote Sens.*, vol. 41, no. 9, pp. 1986–1995, Sep. 2003.
- [54] R. Guida, A. Iodice, and D. Riccio, "Height retrieval of isolated buildings from single high-resolution SAR images," *IEEE Trans. Geosci. Remote Sens.*, vol. 48, no. 7, pp. 2967–2979, Jul. 2010.
- [55] B. Aiazzi, L. Alparone, F. Argenti, S. Baronti, T. Bianchi, and A. Lapini, "An unsupervised method for quality assessment of despeckling: An evaluation on COSMO-SkyMed data," *Proc. SPIE*, vol. 8179, p. 81790D, Oct. 2011.
- [56] G. Di Martino, A. Iodice, D. Riccio, and G. Ruello, "Imaging of fractal profiles," *IEEE Trans. Geosci. Remote Sens.*, vol. 48, no. 8, pp. 3280–3289, Aug. 2010.
- [57] G. Di Martino, D. Riccio, and I. Zinno, "SAR imaging of fractal surfaces," *IEEE Trans. Geosci. Remote Sens.*, vol. 50, no. 2, pp. 630–644, Feb. 2012.
- [58] D. Brunner, G. Lemoine, L. Bruzzone, and H. Greidanus, "Building height retrieval from VHR SAR imagery based on an iterative simulation and matching technique," *IEEE Trans. Geosci. Remote Sens.*, vol. 48, no. 3, pp. 1487–1504, Mar. 2010.



Gerardo Di Martino (S'06–M'09) was born in Naples, Italy, on June 22, 1979. He received the Laurea Degree (*cum laude*) in telecommunication engineering and the Ph.D. degree in electronic and telecommunication engineering from the University of Naples Federico II, in 2005 and 2009, respectively.

He received grants from the University of Naples to be spent at the Department of Biomedical, Electronic and Telecommunication Engineering, for research in indoor electromagnetic propagation and localization of unknown transmitters from 2009 to 2010. He worked on a project financed by the Italian Space Agency aimed at the development of techniques for information extraction from high resolution SAR images of urban and natural areas from 2010 to 2012. He is currently a Post-Doctoral Researcher with the Department of Electrical Engineering and Information Technology, University of Naples Federico II, working on a project regarding maritime surveillance with SAR data. His current research interests include microwave remote sensing and electromagnetics, modeling of the electromagnetic scattering from natural surfaces and urban areas, SAR data simulation and information retrieval, and remote sensing techniques for developing countries.



Mariana Poderico was born in Naples, Italy, on January 22, 1984. She received the Degree in telecommunications engineering and the Ph.D. degree in electronic and telecommunications engineering from the University of Naples Federico II, Naples, Italy, in 2008 and 2012, respectively.

Her study and research activity focuses on SAR image denoising.



Giovanni Poggi received the Laurea degree in electronic engineering from the University Federico II of Naples, Italy, in 1988.

He is currently a Professor of telecommunications with the University Federico II of Naples, Italy, Department of Electrical Engineering and Information Technology and Coordinator of the Telecommunication Engineering School. His current research interests are focused on statistical image processing, including compression, restoration, and segmentation of remote-sensing images, both optical and

SAR, and detection of image forgeries.

Prof. Poggi has been an Associate Editor for the IEEE TRANSACTIONS ON IMAGE PROCESSING and *Signal Processing*.



Luisa Verdoliva received the Laurea degree in telecommunications engineering and the Ph.D. degree in information engineering from the University of Naples Federico II, Naples, Italy, in 1998 and 2002, respectively.

She is currently a Researcher with the Department of Electrical Engineering and Information Technology, University of Naples Federico II. Her current research interests include image processing, particularly denoising and compression of remote sensing images.



Daniele Riccio (M'91–SM'99) was born in Naples, Italy. He received the Laurea Degree (*cum laude*) in electronic engineering from the Università di Napoli Federico II, Naples, Italy, in 1989.

He is currently a Professor of electromagnetic theory and remote sensing with the University of Napoli Federico II, Department of Electrical Engineering and Information Technology. He is a member of the Cassini Radar Science Team. He was a Research Scientist with the Italian National Council of Research (CNR), Institute for Research on

Electromagnetics and Electronic Components. He also was a Guest Scientist with the German Aerospace Center (DLR), Munich, Germany, in 1994 and 1995, and a Visiting Professor with the Universitat Politècnica de Catalunya, Barcelona, Spain, in 2006. He has authored three books, including *Scattering, Natural Surfaces and Fractals*, 2007, and more than 300 papers. His current research interests include microwave remote sensing, electromagnetic scattering, synthetic aperture radar with emphasis on sensor design, data simulation and information retrieval, as well as the application of fractal geometry to remote sensing.

Prof. Riccio was the recipient of the 2009 Sergei A. Schelkunoff Transactions Prize Paper Award for the best paper published in 2008 on the IEEE TRANSACTIONS ON ANTENNAS AND PROPAGATION. He is an Associate Editor for the journals *Remote Sensing*, *Sensors*, *The Open Remote Sensing Journal* and *Applied Remote Sensing Journal*, participates to technical committees of international symposia on electromagnetics and remote sensing, is Principal Investigator for international research projects on exploitation of remote sensing data and design of synthetic aperture radars.